Online Impedance Regulation Techniques for Compliant Humanoid Balancing

Emmanouil Spyrakos-Papastavridis[1], Navvab Kashiri[2], Peter R. N. Childs[1],
and Nikos G. Tsagarakis[2]

***Abstract*—This paper presents three distinct techniques, aimed at the online active impedance regulation of compliant humanoid robots, which endeavours to induce a state of balance to the system once it has been perturbed. The presence of passive elastic elements in the drives powering this class of robots leads to under-actuation, thereby rendering the control of compliant robots an intricate task. Consequently, the impedance regulation procedures proposed in this paper directly account for these elastic elements. In order to acquire an indication of the robot's state of balance in an online fashion, an energy (Lyapunov) function is introduced, whose sign then allows one to ascertain whether the robot is converging to or diverging from, a desired equilibrium position. Computing this function's time derivative unequivocally gives the energy-injecting nature of the active stiffness regulation, and reveals that active damping regulation has no bearing on the system's state of stability. Furthermore, the velocity margin notion is interpreted as a velocity value beyond which the system's balance might be jeopardised, or below which the robot will be guaranteed to remain stable. As a result, the unidirectional and bidirectional impedance optimization methods rely upon the use of bounds that have been defined based on the energy function's derivative, in addition to the velocity margin. Contrarily, the third technique's functionality revolves solely around the use of Lyapunov Stability Margins (LSMs). A series of experiments carried out using the COmpliant huMANoid (COMAN), demonstrates the superior balancing results acquired when using the bidirectional scheme, as compared to utilizing the two alternative techniques.**

I. Introduction

THE topic of bipedal robot balancing has been studied extensively, since it is unquestionably the single most fundamental property whose absence renders a robot incapable of performing any kind of task. A field of research has arisen aiming at systematizing the way through which a humanoid robot's balance is evaluated, with [1] being among the most seminal works, as it introduced the Zero-Moment-Point (ZMP) concept. Strictly speaking, the ZMP describes a point existing under the robot's feet whose position defines the system's overall stability, with a range of possible ankle torque and reaction force combinations yielding a stable robot configuration, which ensures the point's residing within the confines of the convex hull of the support polygon. The literature is replete with works pertaining to humanoid balancing, which are contingent upon the use of this criterion, with quintessential examples of such techniques presented in [2]-[4].

[1]E. Spyrakos-Papastavridis and P. R. N. Childs are with the Dyson School of Design Engineering, Imperial College London, South Kensington, London, SW7 2AZ, UK, {e.spyrakos-papastavridis, p.childs} at imperial.ac.uk
[2]N. Kashiri and N. G. Tsagarakis are with the Department of Advanced Robotics, Istituto Italiano di Tecnologia, via Morego, 30, 16163 Genova, Italy {navvab.kashiri, nikos.tsagarakis} at iit.it

The work described in [2] proposes a method aimed at rendering a humanoid passive, which exploits a combination of translating the ground reaction forces (GRFs) to joint torques, and gravity compensation control, thus obviating the requirement for inverse dynamics calculations. The work described in [3] manifested itself as a breakthrough, as it served the purpose of introducing the Linear Inverted Pendulum Model (LIPM) that significantly facilitated the humanoid control problem, while its simplicity also served as a valuable analysis tool that was exploited in various works thereafter. [4] delves into the use of such simplified models for the purpose of developing an array of decision surfaces, permitting the selection of the most appropriate model and strategy, at a given point in time, that would be capable of reinstating the system's desired state of balance. A closely related balancing criterion referred to as the CoP, has also been investigated due to its frequent equivalence with the ZMP, with [5] analysing the discrepancies arising when comparing the actual CoP measurements, to ZMP values computed using two distinct techniques.

In an attempt to produce robots capable of emulating natural, human-like behaviour during interaction with their respective environments, roboticists have striven to engineer appropriate impedance control schemes [6] that would be conducive to this objective. A natural consequence of this effort has been the employment of such control methods on bipedal robots [7]-[14], for the purpose of realizing a desired interaction with the environment, which may potentially lead to successful execution of the specified tasks, provided that the impedance levels are appropriately controlled. As regards humanoid balance maintenance, its achievement necessitates impedance regulation capable of endowing the system with terrain adaptability, in addition to accurate and rapid convergence towards a desired equilibrium point. The use of fixed gain impedance controllers would preclude the coexistence of both features simultaneously, which consequently gives rise to the need for a systematic approach to adjusting a robot's impedance values. However, such an approach ought to incorporate the balancing constraints, as their exclusion would be tantamount to utilising constant gain controllers. Thus, the work described herein has striven to encapsulate real-time analytical impedance selection, and balance monitoring into a single, unified algorithm.

It has been established that admittance control schemes could be utilized for the attenuation of landing forces [7], via

measurement of the actual force values that in turn allows for a calculation of the desired foot position, while an additional time domain approach targeted at improved environmental interaction is provided in [8]. Conversely, [9][10] outline methodical, analytical strategies for the regulation of the system's impedance during the distinct walking phases. [11][12] propose impedance control schemes for bipedal robots, whereby the swing leg's foot and hip impedance parameters increase considerably upon contact with the environment, in order to absorb the landing forces and maintain contact with the ground. The methodology expounded in [13], epitomises the effectiveness of utilising compliance control techniques and operational space control, as regards a robot's interaction with its environment. Additionally, there is ongoing research into balancing techniques that explicitly consider the physical ZMP constraints, through the monitoring of a particular control law, thereby facilitating the tuning/optimisation of the system's viscoelasticity parameters [14][15]. Further work on dynamics computations for operational space control, is provided in [16].

Despite the fact that all the afore-described works deal solely with humanoid robots comprising 'stiff' joints, the recent trend entailing the development of bipeds powered by series elastic actuators, has led to the devise of balancing and walking strategies for this class of humanoids [17][18]. [17] details an approach that enables precise control of COMAN's compliant joints [19]-[20], whilst [18] presents a CPG-based controller for the same robot.

It is noticeable that the majority of works have dealt with ankle strategies relying upon the LIPM. Contrarily, the technique proposed in this paper is targeted at the real-time regulation of the impedance [22] of all the individual sagittal joints, thus allowing for the knee and hip joints' contribution to the robot's overall perturbation rejection performance. In summary, the proposed methodology unifies the benefits associated with low and high impedance controllers, as a means of ensuring amplified impact tolerance, contact maintenance, and convergence to a desired equilibrium. The content of this paper serves as an extension to [23], from which it differs by virtue of providing Appendices that accurately outline the steps involved in the stability analysis proof. Additionally, it offers an accompanying passivity proof that is germane to the experimental push recovery results, since they are directly involved with the application of external disturbances to the robot. This supplementary feature consolidates the theoretical facets of the work, and renders it suitable for application to robots directly interacting with their surroundings. Two additional push recovery techniques, namely the unidirectional optimization and the LSM-based tuning technique, are also introduced herein, as their direct comparison with the proposed method serves as a metric of the latter's performance. Therefore, the contributions presented herein are the following:

- Analytical methods for the tuning of a balancing humanoid's joint impedances in real time.
- A novel balance monitoring variable allowing for a replacement of challenging balance constraints with ones that are swiftly computed in real time.
- The merging of an impedance optimization technique with the proposed velocity-based balance variable.
- Mathematical analyses which are adduced to prove the system's stability and passivity.
- A direct comparison between the proposed method, and two correlated, alternative approaches.

The rest of the paper is structured as follows; section II describes the double support dynamics and the associated energy function, section III introduces the velocity margin concept as a balance monitor, section IV provides a detailed explanation of the bidirectional impedance regulation algorithm, section V offers a thorough description of the alternative impedance tuning techniques, section VI presents the impedance regulation experimental results, and finally section VII gives the conclusions.

II. Compliant Double Support Dynamics and Variable Impedance Energy Function

This section introduces the mathematical model describing the dynamics of the system, which shall be considered throughout the paper, for the development of the associated control algorithms and balancing techniques.

For the double support case, a $j = 3$ -DOF robot with $n = 2$ drives for each DOF is considered, where the total number of drives is $n \times j = 6$. The link and motor dynamics[1] may then be described as follows [24]:

$$\mathbf{M_J}(\boldsymbol{q})\ddot{\boldsymbol{q}} + \mathbf{C}(\boldsymbol{q}, \dot{\boldsymbol{q}})\dot{\boldsymbol{q}} + \mathbf{S_m^T K}(\mathbf{S_m}\boldsymbol{q} - \boldsymbol{\theta}) = \boldsymbol{\tau_g}(\boldsymbol{q}) + \boldsymbol{\tau_{ex}}, \quad (1)$$

$$\mathbf{J}\ddot{\boldsymbol{\theta}} + \mathbf{D}\dot{\boldsymbol{\theta}} - \mathbf{K}\mathbf{S_m}\boldsymbol{q} + \mathbf{K}\boldsymbol{\theta} = \boldsymbol{\tau_m}, \quad (2)$$

where $\boldsymbol{q} \in \mathbb{R}^j$ and $\boldsymbol{\theta} \in \mathbb{R}^n$ denote the link and motor positions, $\mathbf{M_J}(\boldsymbol{q}) \in \mathbb{R}^{j \times j}$ and $\mathbf{C}(\boldsymbol{q}, \dot{\boldsymbol{q}}) \in \mathbb{R}^{j \times j}$ represent the inertia and Coriolis/centripetal matrices respectively, $\boldsymbol{\tau_g}(\boldsymbol{q}) \in \mathbb{R}^j$ is the gravity torque vector, $\boldsymbol{\tau_m} \in \mathbb{R}^n$ is the actuation torque vector and $\boldsymbol{\tau_{ex}} \in \mathbb{R}^j$ symbolises the vector of external forces. $\mathbf{K} \in \mathbb{R}^{n \times n}$ is a diagonal matrix with positive entries representing the passive spring stiffness between the motors and the robot links, while $\mathbf{J}, \mathbf{D} \in \mathbb{R}^{n \times n}$ are the motor inertia and damping. $\mathbf{S_m} \in \mathbb{R}^{n \times j}$ is a selection matrix that serves the purpose of selecting the appropriate actuators for every link ($j < n$ is considered herein), with its columns associated to the system's motors and its rows to the system's joints. Assuming that the first n_1 drives are connected to link 1, the next n_2 drives are connected to link 2, and so forth, then $\mathbf{S_m^T}$ possesses the following form:[1]

[1] In this article, matrices, vectors, scalars and operators are represented in bold, bold italic, italic, and regular letters respectively.

$$\mathbf{S_m^T} = \begin{bmatrix} \underbrace{1\,1\cdots1}_{m_1} & 0 & \cdots & 0 \\ 0 & \underbrace{1\,1\cdots1}_{m_2} & \cdots & 0 \\ \vdots & \vdots & \ddots & \vdots \\ 0 & 0 & \cdots & \underbrace{1\,1\cdots1}_{m_n} \end{bmatrix}.$$

However, the above equation is transformed into an identity matrix if the system is equal actuated ($j = n$), while $j > n$ refers to redundant kinematic actuation.

Remark 1: The work herein has revolved around the use of a model describing a simple form of a closed kinematic chain, as it befits the characteristics of the pertinent experimental platform, since the objective of this work has been to demonstrate the development of a systematic method for whole-body impedance gain tuning. Nevertheless, the proposed control technique can be adapted to a range of closed kinematic chain models, when the system dynamics is represented in the form described in [25].

The over-actuation of the double support phase necessitates a lower-DOF model representation, which will however account for all the actuators. For instance, given a bipedal robot possessing three-DOF legs, as depicted in Fig. 1, the three-DOF double support gravity vector is arranged as follows:

$$\boldsymbol{\tau_g} = [\boldsymbol{\tau_a} \quad \boldsymbol{\tau_k} \quad \boldsymbol{\tau_h}]^T, \tag{3}$$

with $\boldsymbol{\tau_a}, \boldsymbol{\tau_k}, \boldsymbol{\tau_h}$ representing the ankle, knee and hip torques respectively. An imperative property of the gravity vector, to be used in subsequent sections, is [26]:

$$\left\| \frac{\partial \boldsymbol{\tau_g}(\boldsymbol{q})}{\partial \boldsymbol{q}} \right\| = \left\| \frac{\partial^2 U_g(\boldsymbol{q})}{\partial \boldsymbol{q}^2} \right\| \leq \alpha, \tag{4}$$

for some $\alpha > 0$; where $U_g(\boldsymbol{q})$ denotes the potential energy due to gravity, $\boldsymbol{\tau_g}(\boldsymbol{q}) = -\left(\partial U_g(\boldsymbol{q})/\partial \boldsymbol{q}\right)^T$ and the operator norm $\|A\| = \max\{\|Ax\|/\|x\|\}$ is considered.
The low-level joint controller is based upon gravity compensation control, employing motor feedback, thus the associated control law may be represented as follows [27]:

$$\boldsymbol{\tau_m} = \mathbf{K_P}(\mathbf{S_m}\boldsymbol{q_d} - \boldsymbol{\theta}) - \mathbf{K_D}\dot{\boldsymbol{\theta}} + \boldsymbol{u_{gc}}, \tag{5}$$

where $\boldsymbol{u_{gc}} \in \mathbb{R}^n$ is the gravity compensation term and $\boldsymbol{q_d} \in \mathbb{R}^j$ is the desired position, while $\mathbf{K_P} \in \mathbb{R}^{n\times n}$, $\mathbf{K_D} \in \mathbb{R}^{n\times n}$ are the diagonal, positive definite motor position and motor velocity feedback gain matrices, i.e. $\mathbf{K_P} = \mathrm{diag}(K_{P,1}, \ldots K_{P,n})$, $\mathbf{K_D} = \mathrm{diag}(K_{D,1}, \ldots K_{D,n})$, with $\mathrm{diag}([.])$ returning the diagonal matrix of the vector $[.]$. For the double support model, $\boldsymbol{u_{gc}}$ is given by:

$$\boldsymbol{u_{gc}} = -(\mathbf{K_P}\mathbf{K}^{-1} + \mathbf{I})(\mathbf{S_m^T})^{+}\boldsymbol{\tau_g}(\boldsymbol{q_d}), \tag{6}$$

where $\boldsymbol{q}$ has been replaced with $\boldsymbol{q_d}$ since a desired gravity compensation controller is being considered, in contrast to that utilised in [28], while $(\mathbf{S_m^T})^{+}$ denotes the Moore-Penrose pseudoinverse of $\mathbf{S_m^T}$.

Remark 2: Equations (5) and (6) may be represented in a similar form to the conventional PD plus gravity compensation controllers, through a series of calculations that commence with a substitution of (6) into (5), as shown below:

$$\boldsymbol{\tau_m} = \mathbf{K_P}(\mathbf{S_m}\boldsymbol{q_d} - \boldsymbol{\theta}) - \mathbf{K_D}\dot{\boldsymbol{\theta}} - (\mathbf{K_P}\mathbf{K}^{-1} + \mathbf{I})(\mathbf{S_m^T})^{+}\boldsymbol{\tau_g}(\boldsymbol{q_d}).$$

Since however $(\mathbf{S_m^T})^{+}\boldsymbol{\tau_g}(\boldsymbol{q_d}) = -\mathbf{K}(\boldsymbol{\theta_d} - \mathbf{S_m}\boldsymbol{q_d})$ [24], then:

$$\boldsymbol{\tau_m} = \mathbf{K_P}(\mathbf{S_m}\boldsymbol{q_d} - \boldsymbol{\theta}) - \mathbf{K_D}\dot{\boldsymbol{\theta}} + (\mathbf{K_P}\mathbf{K}^{-1} + \mathbf{I})\mathbf{K}(\boldsymbol{\theta_d} - \mathbf{S_m}\boldsymbol{q_d})$$

$$\boldsymbol{\tau_m} = \mathbf{K_P}(\mathbf{S_m}\boldsymbol{q_d} - \boldsymbol{\theta}) - \mathbf{K_D}\dot{\boldsymbol{\theta}} + \mathbf{K_P}(\boldsymbol{\theta_d} - \mathbf{S_m}\boldsymbol{q_d}) + \mathbf{K}(\boldsymbol{\theta_d} - \mathbf{S_m}\boldsymbol{q_d}),$$

which leads to:

$$\boldsymbol{\tau_m} = \mathbf{K_P}(\boldsymbol{\theta_d} - \boldsymbol{\theta}) - \mathbf{K_D}\dot{\boldsymbol{\theta}} + \mathbf{K}(\boldsymbol{\theta_d} - \mathbf{S_m}\boldsymbol{q_d}),$$

where the final term may be replaced by $-(\mathbf{S_m^T})^{+}\boldsymbol{\tau_g}(\boldsymbol{q_d})$, yielding:

$$\boldsymbol{\tau_m} = \mathbf{K_P}(\boldsymbol{\theta_d} - \boldsymbol{\theta}) - \mathbf{K_D}\dot{\boldsymbol{\theta}} - (\mathbf{S_m^T})^{+}\boldsymbol{\tau_g}(\boldsymbol{q_d}).$$

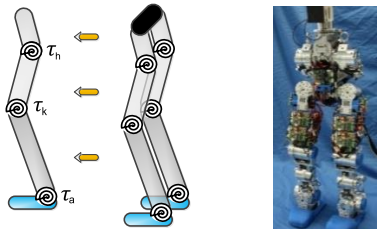

Figure 1. COMAN lower body and corresponding double support model.

By accounting for the closed-loop system's steady state equations, we can define the overall stiffness matrix

$$\mathbf{T_D} = \begin{bmatrix} \mathbf{S_m^T}\mathbf{K}\mathbf{S_m} & -\mathbf{S_m^T}\mathbf{K} \\ -\mathbf{K}\mathbf{S_m} & \mathbf{K} + \mathbf{K_P} \end{bmatrix} \in \mathbb{R}^{(n+j)\times(n+j)}, \tag{7}$$

where the **D** subscript denotes the double support phase, and plays a pivotal role in the stability analysis, since its satisfaction of certain conditions ensures the uniqueness of the equilibria.
By gathering the afore-presented terms $((1), (2), (7))$, whilst nullifying the velocities and accelerations $((1), (2))$ in the absence of external forces, the system's closed-loop equations may be expressed as follows:

$$\mathbf{T_D}\begin{bmatrix} \boldsymbol{q} - \boldsymbol{q_d} \\ \boldsymbol{\theta} - \boldsymbol{\theta_d} \end{bmatrix} = \begin{bmatrix} \boldsymbol{\tau_g}(\boldsymbol{q}) - \boldsymbol{\tau_g}(\boldsymbol{q_d}) \\ 0 \end{bmatrix}.$$

Thus, the above equation indicates that the closed-loop system's potential energy behaviour is defined by both a

gravitational, and a stiffness term. In order to ensure that this pseudo-net-potential energy is strictly convex, the following condition ought to be satisfied:

$$\lambda_{\mathrm{m}}(\mathbf{T_D}) > \alpha, \tag{8}$$

where $\lambda_m(.)$ denotes the minimum eigenvalue/component of a given matrix/vector.
Additionally, the desired motor positions $\boldsymbol{\theta_d} \in \mathbb{R}^n$ are related to the desired link positions by:

$$\boldsymbol{\theta_d} = \mathbf{S_m} \boldsymbol{q_d} - \mathbf{K}^{-1}(\mathbf{S_m^T})^{+} \boldsymbol{\tau_g}(\boldsymbol{q_d}). \tag{9}$$

In contrast to the majority of relevant controllers, it is noteworthy that this work considers the real-time variation of the diagonal elements of the $\mathbf{K_P}$ and $\mathbf{K_D}$ matrices, paving the way for the introduction of the two pertinent theorems, which are stated below.

Theorem 1: By inserting (5) and (6) into the system described by (1) and (2), and considering a Lyapunov function inspired by [27], of the form:

$$V_T = \frac{\boldsymbol{q_F^T} \mathbf{M} \boldsymbol{q_F}}{2} + \frac{\boldsymbol{q_E^T} \mathbf{T_D} \boldsymbol{q_E}}{2} + U_g(\boldsymbol{q}) - U_g(\boldsymbol{q_d}) + \boldsymbol{q_E^T} \begin{bmatrix} \boldsymbol{\tau_g}(\boldsymbol{q_d}) \\ 0 \end{bmatrix}, \tag{10}$$

where $\boldsymbol{q_F} = \begin{bmatrix} \boldsymbol{q} \\ \boldsymbol{\theta} \end{bmatrix}$, $\boldsymbol{q_{F_d}} = \begin{bmatrix} \boldsymbol{q_d} \\ \boldsymbol{\theta_d} \end{bmatrix}$, $\boldsymbol{q_E} = (\boldsymbol{q_F} - \boldsymbol{q_{F_d}}), \mathbf{M}(\boldsymbol{q}) = \begin{bmatrix} \mathbf{M_J}(\boldsymbol{q}) & 0 \\ 0 & \mathbf{J} \end{bmatrix}$; while assuming that $\lambda_{\mathrm{m}}(\mathbf{T_D}) \geq \alpha$, and $\mathbf{T_D}$ is a time-varying matrix, there exists a unique equilibrium solution at $[\boldsymbol{q_d^T} \quad \boldsymbol{\theta_d^T} \quad 0 \quad 0]$. This equilibrium is globally asymptotically stable when $\mathbf{T_D}$ is a constant matrix, and/or when $\mathbf{T_D}$ is time-varying provided that either the system's stiffness decreases, or that while the stiffness is increasing the following condition is satisfied:

$$\dot{\boldsymbol{q}}_{\boldsymbol{F}}^{\boldsymbol{T}} \boldsymbol{\eta} \dot{\boldsymbol{q}}_{\boldsymbol{F}} \geq \frac{1}{2} \boldsymbol{q}_{\boldsymbol{E}}^{\boldsymbol{T}} \dot{\mathbf{T}}_{\mathbf{D}} \boldsymbol{q}_{\boldsymbol{E}},$$

where $\boldsymbol{\eta} = \mathrm{H}(\mathbf{D} + \mathbf{K_D})$ is the overall damping matrix and $\dot{\mathbf{T}}_{\mathbf{D}}$ signifies the time derivative of the $\mathbf{T_D}$ matrix. The matrix operator, H(.), constructing an $(n+j)\times(n+j)$ matrix from the $n\times n$ matrix (.), is expressed as follows:

$$\mathrm{H}(\mathbf{D} + \mathbf{K_D}) = \begin{bmatrix} 0_{j\times j} & 0_{j\times n} \\ 0_{n\times j} & \mathbf{D} + \mathbf{K_D} \end{bmatrix},$$

where $0_{\kappa\times\vartheta}$ symbolizes a zero matrix of dimension $\kappa\times\vartheta$, and $\mathrm{H}^{-1}\left(\begin{bmatrix} 0_{j\times j} & 0_{j\times n} \\ 0_{n\times j} & \mathbf{D} + \mathbf{K_D} \end{bmatrix}\right) = \mathbf{D} + \mathbf{K_D}$.
The mathematical stability proof pertaining to the above theorem, is delineated in Appendix A.

Theorem 2: By inserting (5) and (6) into the system described by (1) and (2), whilst assuming that $\lambda_{\mathrm{m}}(\mathbf{T_D}) \geq \alpha$, and $\mathbf{T_D}$ is a time-varying matrix, then the closed-loop system remains passive either when the stiffness decreases, or when the $\dot{\boldsymbol{q}}_{\boldsymbol{F}}^{\boldsymbol{T}} \boldsymbol{\eta} \dot{\boldsymbol{q}}_{\boldsymbol{F}} \geq \frac{1}{2} \boldsymbol{q}_{\boldsymbol{E}}^{\boldsymbol{T}} \dot{\mathbf{T}}_{\mathbf{D}} \boldsymbol{q}_{\boldsymbol{E}}$ condition is satisfied, in the presence of increscent stiffness values. An analytical demonstration of the proof elicitation is provided in Appendix B.

III. Balance Monitoring using The Velocity Margin

This section focuses on providing a description of the balance monitoring technique that revolves around the use of the velocity margin, which is introduced both conceptually and mathematically.

A. State of Balance Detection

A compliant humanoid robot assuming a standing configuration, with zero ankle torques yielding $X_{CoP} = 0$, shall inevitably diverge with respect to the equilibrium once an impulsive impact has been applied to its structure. Under the assumption that a balanced state ensues the disturbance, then the system will most likely oscillate around the equilibrium position, before coming to a halt at the desired configuration. The manner in which this transpires shall be contingent upon the system's dynamics, with the springs potentially playing a vital role in the robot's perturbation absorption performance during the post-impact phase. It is thus essential to contrive a method of determining whether the robot is converging or diverging, at a given point in time. One means of accomplishing this goal is through the monitoring of the energy variation between samples, E_{SGN}, which should evidently occur in an online fashion, i.e. the robot diverges when $E_{SGN} > 0$ and it converges when $E_{SGN} < 0$. Therefore, the formula provided below:

$$E_{SGN} = \mathrm{sgn}\big(V_T(i) - V_T(i-1)\big), \tag{11}$$

gives a scalar value that is indicative of the system's state of balance, at every sample. A negative E_{SGN} signifies convergence, whilst a positive E_{SGN} implies divergence (Fig. 2), which is initiated by the application of an external force to the system.

B. Velocity Margin Formulation

This term is initially reminiscent of the familiar 'velocity-based stability margin' expression, which was coined in [29], and describes a margin that accounts for a humanoid robot's dynamical parameters, including the CoM velocity and angular momentum. However, the velocity margin to be introduced in the subsequent lines, is a critical velocity value which when exceeded could potentially lead to system instability, or a value below which the robot's stability is ensured. Ideally, the robot should perform a pre-emptive action prior to the occurrence of an unstable state, which totally justifies the desire for a margin that is slightly conservative. In order to acquire such a variable, the CoP-Energy relationship derived in [30] could be shaped appropriately to yield a critical velocity value, as opposed to the critical energy value that it initially described in [30]. This is achieved via the formula:

$$V_T \geq \frac{\delta}{2(n_M + 1)} k_v, \tag{12}$$

where $k_v = \left(\frac{|X_{CoP} - X_{CoP_d}| m_T g}{\|\boldsymbol{G}\mathbf{S}_\mathbf{m}^\mathbf{T}\mathbf{K}\|}\right)^2$, $\delta = \lambda_{\mathrm{m}}(\mathbf{T_D}) - \alpha$, with m_T, g, X_{CoP}, X_{CoP_d} being the robot's total mass, gravitational acceleration constant, actual CoP position, and desired CoP position respectively. X_{CoP} is assigned its value by virtue of knowing the dimensions of the support polygon, while X_{CoP_d} is defined based on either a precomputed desired configuration, a balancing controller, or a trajectory generator. Moreover, $\|\mathbf{S_m}\| = \sqrt{n_M}$, $n_M = \max_{1 \le i \le j}(\mathrm{n_i})$, $\boldsymbol{G} \in \mathbb{R}^j$ is a constant selection vector which implies that the denominator of the scalar k_v, corresponds to the overall stiffness of the ankle joints. Consequently, the right-hand side of equation (12) denotes a critical energy value, which when surpassed by the magnitude of V_T, might indicate the arousal of an unstable state. A derivation of equation (12), termed the Lyapunov Stability Margin (LSM), has been provided in Appendix C, in order to clarify the mathematical logic that governs its operation. Although this is a sufficient rather than a necessary condition, one should be circumspect about exceeding the associated bound, and preferably treat it as a safety constraint.

By then assuming that $V_T = \frac{1}{2}\dot{\boldsymbol{q}}_F^{\boldsymbol{T}}\mathbf{M}(\boldsymbol{q})\dot{\boldsymbol{q}}_F + V_P$, wherein $V_P = \frac{\boldsymbol{q}_E^{\boldsymbol{T}}\mathbf{T_D}\boldsymbol{q}_E}{2} + U_g(\boldsymbol{q}) - U_g(\boldsymbol{q}_d) + \boldsymbol{q}_E^{\boldsymbol{T}}\begin{bmatrix}\boldsymbol{\tau}_g(\boldsymbol{q}_d)\\ 0\end{bmatrix}$ denotes the potential energy, equation (12) may be expressed in the manner shown below:

$$\frac{1}{2}\dot{\boldsymbol{q}}_F^{\boldsymbol{T}}\mathbf{M}\dot{\boldsymbol{q}}_F + V_P \ge \frac{\delta}{2(n_M+1)}k_v. \tag{13}$$

Segregating the kinetic energy term, results in:

$$\|\mathbf{M}\|\|\dot{\boldsymbol{q}}_F\|^2 \ge \frac{\delta}{(n_M+1)}k_v - 2V_P, \tag{14}$$

while rearranging (14) w.r.t the velocity term then yields:

$$v \ge \sqrt{\frac{1}{\|\mathbf{M}\|}\left(\frac{\delta}{(n_M+1)}k_v - 2V_P\right)}, \tag{15}$$

where $\|\dot{\boldsymbol{q}}_F\|$ has been substituted for the velocity margin variable, v. Equation (15) is not explicitly defined based on the slack, despite representing a margin, since this property is implicitly accounted for through the k_v and V_P values that (15) encompasses.

The right-hand side of the above equation represents a critical velocity value, the exceedance of which may potentially correspond to the system's possession of an unstable state, i.e. the system is about to fall. However, the validity of this condition is dependent upon whether the aforesaid term remains positive, which is only the case if:

$$\frac{\delta}{(n_M+1)}k_v \ge 2V_P, \tag{16}$$

and should be respected within a particular region encircling the equilibrium. It may then be stated that v is a conditional velocity margin, whose values are indicative of the system's balance only when (16) is satisfied.

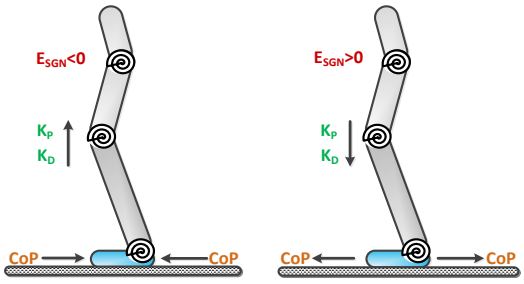

Figure 2. Energy variations are positive during divergent phase (CoP diverging) and negative during convergent phase (CoP converging).

To summarize, equation (15) implies that for a specific configuration, or energy value, there exists an associated critical velocity value, below which the robot is bound to remain stable. Nevertheless, it is worth mentioning that a judicious interpretation may be attached to the velocity margin, solely when its value is positive, since a negative value could insinuate that either the robot's state of balance has actually been compromised, or that it has exceeded the region corresponding to the LSM, described by (12). Since the velocity margin is only conditionally valid (i.e. within a specific discoidal region in the support polygon), as it is associated with the conservative LSM quantity, its possession of negative values indicates that its region of validity has been exceeded. This aspect is crucial in its operation, since it allows it to serve as a safety margin, as opposed to a definite indicator of instability, which would hinder the algorithm's capability of taking pre-emptive actions to prevent the arousal of dangerous states. To elaborate, the velocity margin possesses its maximum value when the robot is at rest, and is assigned a zero value at the boundaries of the validity region. This notion may alternatively be perceived as follows "For a given robot configuration, what velocity magnitude would be required in order to induce an unbalanced state to the system?"

IV. Impedance Parameter Tuning

This section explains the mechanics of the bidirectional online impedance tuning algorithm, and presents the mathematical tools required for the realisation of the proposed methodology.

The propounded impedance regulation scheme's operation, revolves around the optimization of the system's impedance levels, that is in turn dictated by the robot's instantaneous state of balance, monitored by virtue of the energy variation equation described by (11). As illustrated in Fig. 3, the algorithm attempts to minimize the robot's impedance in response to an energy increase that typically ensues an external disturbance, in order to withstand as large a perturbation as possible. This entails a minimisation of the system's stiffness and damping levels by utilising certain physically-motivated constraints, in addition to defining appropriate bounds ensuring that the proposed stiffness and

damping optimization procedures yield values that conform to the stability-related conditions. Additionally, the damping value optimisation is directly contingent upon the previously mentioned velocity margin's real-time evolution. Conversely, the impedance level is maximized once an energy decrease is detected, for the purpose of amplifying the system's convergence capability. This procedure comprises online increases of the stiffness and damping values that endeavour to ensure the preservation of both stability and passivity, whilst accounting for the actuators' physical limitations.

A. Online Stiffness Optimization

The establishment of the definitions of both the balancing strategy and the velocity margin, has laid the foundations for the formulation of a control method.

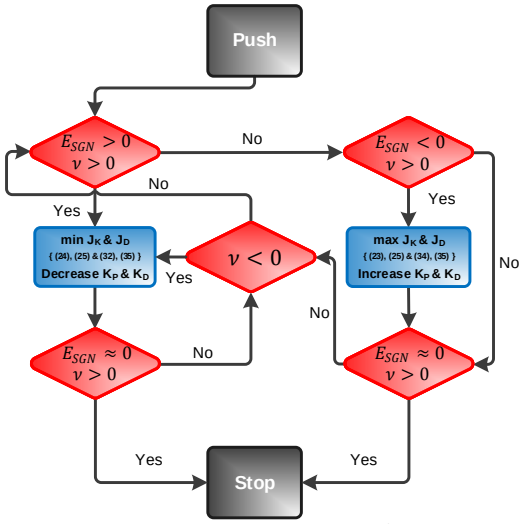

Figure 3. Impedance regulation scheme flowchart.

As logic dictates, the mechanics of the online stiffness tuning technique shall firstly be introduced, since a lower bound may immediately be derived by constraining the magnitude of the $\mathbf{K_P}$ matrix in accordance with the value of α. However, since the ultimate goal is to acquire as low a stiffness as possible once the system diverges from a desired equilibrium, coupled with the fact that (8) may be expressed as[2]

$$\lambda_{\mathrm{M}}(\mathrm{H}(\mathbf{K_P})) \geq \alpha - \lambda_{\mathrm{M}}(\mathbf{K_T}), \tag{17}$$

with $\lambda_{\mathrm{M}}(.)$ denoting the maximum eigenvalue, then the minimum stiffness gain scalar value, $k_{P_{min}}$, may be computed by utilizing the formula:

$$k_{P_{min}} = \left(\alpha - \lambda_{\mathrm{M}}(\mathbf{K_T})\right). \tag{18}$$

The matrix containing the passive stiffness elements, is represented through the equation:

$$\mathbf{K_T} = \begin{bmatrix} \mathbf{S_m^T K S_m} & -\mathbf{S_m^T K} \\ -\mathbf{K S_m} & \mathbf{K} \end{bmatrix} \in \mathbb{R}^{(n+j)\times(n+j)},$$

[2] It can be shown that $\lambda_{\mathrm{M}}(\rho + \chi) \leq \lambda_{\mathrm{M}}(\rho) + \lambda_{\mathrm{M}}(\chi)$ ([31]).

Furthermore, an upper bound can be attained by calculating the $\mathbf{K_D}$ gain value, denoted by $k_{D_{max}}$, that would lead to saturation of the input torque signal, under the assumption that the saturation damping gain can be described in the following manner:

$$k_{D_{max}} = 2\xi_d \sqrt{k_{P_{max}} \|\mathbf{J}\|}, \tag{19}$$

wherein ξ_d signifies the desired damping ratio, whereas $k_{P_{max}} = \|\mathbf{K_P}\|$ is the maximum active stiffness value. The acquirement of the maximal attainable stiffness value, $k_{P_{max}}$, may be performed by incorporating (19) into (5), and taking into account the maximum achievable actuation torques that prevent the saturation of the input torque signal, it can be shown that:

$$\begin{aligned} \|\boldsymbol{\tau_m}\| = k_{P_{max}} q_{E_{err}} + \left\|\boldsymbol{u_{gc}}\right\| \\ + 2\xi_d \sqrt{k_{P_{max}} \|\mathbf{J}\|} \left\|\dot{\boldsymbol{\theta}}\right\|, \end{aligned} \tag{20}$$

where the $\|\boldsymbol{\tau_m}\|$ and $\|\mathbf{J}\|$ values are known beforehand according to the joint torque saturation values and the motor's electromechanical properties, whereas $\left\|\dot{\boldsymbol{\theta}}\right\|$, $q_{E_{err}} = \|\mathbf{S_m} \boldsymbol{q_d} - \boldsymbol{\theta}\|$ and $\left\|\boldsymbol{u_{gc}}\right\|$ are assigned their respective values in real time, using sensory measurements. For the derivation of equation (19) above, the norms of the elements on either side are computed while accounting solely for the equality condition, resulting in the production of the largest attainable gain magnitudes exploiting the full capacity of the actuators. By then substituting an inherently positive variable, A^2, such that $A^2 = k_{P_{max}}$, in the above equation (19), the following expression is generated:

$$A^2 q_{E_{err}} + A\left(2\xi_d \sqrt{\|\mathbf{J}\|} \left\|\dot{\boldsymbol{\theta}}\right\|\right) + \left(\left\|\boldsymbol{u_{gc}}\right\| - \|\boldsymbol{\tau_m}\|\right) = 0.$$

The above operation is carried out in view of the fact that the above relationship is quadratic, implying that it can be solved in a straightforward fashion, even though its discriminant's positiveness requires validation on the basis of the standard quadratic equation solution, which should guarantee the provision of a real solution:

$$\xi_d^2 \left\|\dot{\boldsymbol{\theta}}\right\|^2 \|\mathbf{J}\| - q_{E_{err}} \left\|\boldsymbol{u_{gc}}\right\| + q_{E_{err}} \|\boldsymbol{\tau_m}\| > 0. \tag{21}$$

The soundness of the inequality, $\|\boldsymbol{\tau_m}\| \geq \left\|\boldsymbol{u_{gc}}\right\|$, allows for the production of real solutions for the $k_{P_{max}}$ variable, using (20). It may hence be used to generate $k_{P_{max}}$ values, having previously set $\xi_d = 1$, $\xi_d = 0.1$ for the convergent and divergent cases respectively.

The optimization program exploits the overall stiffness term in its original quadratic form, which is compatible with that appearing in the energy function. As the system begins to converge/diverge towards/from an arbitrary equilibrium

point, the $\boldsymbol{q_E^T \mathbf{T_D} q_E}$ stiffness term present in the Lyapunov function (10), should be confined to evolving within certain bounds. However, since the quadratic term inevitably generates scalar values, the associated gains will be incapable of reflecting the robot's mass distribution. To this end, the work herein postulates that a distribution of this nature could be achieved using a gravitational weighting matrix, defined as:

$$\mathbf{W_K} = \text{diag}\left(\frac{\mathbf{S_m}\boldsymbol{\tau_g}(\boldsymbol{q})}{\left\|\mathbf{S_m}\boldsymbol{\tau_g}(\boldsymbol{q})\right\|_1}\right) \in \mathbb{R}^{n\times n}, \tag{22}$$

where $\|.\|_1$ symbolizes the L^1-norm operator, permitting an online calculation of $\left\|\mathbf{S_m}\boldsymbol{\tau_g}(\boldsymbol{q})\right\|_1$.

The stiffness optimisation to be described, has revolved around the use of the overall quadratic stiffness term contained within the Lyapunov function (10), as it is the sole energy variable directly related to the system's stiffness.

The afore-described bounds, (18) and (21), in combination with the weighting matrix, (22), produce two distinct equations, as elaborated below:

- The stiffness energy term can be bounded from above by applying the operator norm to the quadratic function comprising the maximum stiffness gain and the passive elastic elements. Initially, equation (7) is decomposed and presented in terms of its constituents as follows:

$$\mathbf{T_D} = \mathbf{K_T} + \mathrm{H}(\mathbf{K_P}),$$

while the $k_{P_{max}}$ term is subsequently multiplied by $\mathbf{W_K^{-1}}$. The H(.) operator is then used on the resulting matrix, while utilising the property $0 \leq \|\mathbf{W_K}\| \leq 1$, to ensure the production of sufficiently large active stiffness gain values, thereby permitting the statement of the following upper bound, as demonstrated below:

$$\boldsymbol{q_E^T \mathbf{T_D} q_E} \leq \left\|\mathbf{K_T} + \mathrm{H}\left(\mathbf{W_K^{-1}} k_{P_{max}}\right)\right\| \|\boldsymbol{q_E}\|^2,$$

which may be rewritten in the following form:

$$\boldsymbol{q_E^T}\mathrm{H}(\mathbf{K_P})\boldsymbol{q_E} \leq \left\|\mathbf{K_T} + \mathrm{H}\left(\mathbf{W_K^{-1}} k_{P_{max}}\right)\right\| \|\boldsymbol{q_E}\|^2 - \boldsymbol{q_E^T \mathbf{K_T} q_E}. \tag{23}$$

- Obtaining the minimum eigenvalue of the quadratic stiffness term, could then yield a term serving as a lower bound (given that $\|\mathbf{K_P}\| \geq \lambda_{\mathrm{M}}(\mathbf{K_P})\|\mathbf{W_K}\|$) described by the following equation:

$$\lambda_{\mathrm{m}}\left(\mathbf{K_T} + \mathrm{H}\left(\mathbf{W_K} k_{P_{min}}\right)\right)\lambda_{\mathrm{m}}(\boldsymbol{\Phi})^2 \leq \boldsymbol{q_E^T \mathbf{T_D} q_E},$$

which may also be rearranged as follows:

$$\lambda_{\mathrm{m}}\left(\mathbf{K_T} + \mathrm{H}\left(\mathbf{W_K} k_{P_{min}}\right)\right)\lambda_{\mathrm{m}}(\boldsymbol{\Phi})^2 - \boldsymbol{q_E^T \mathbf{K_T} q_E} \leq \boldsymbol{q_E^T}\mathrm{H}(\mathbf{K_P})\boldsymbol{q_E}, \tag{24}$$

where $\boldsymbol{\Phi} \in \mathbb{R}^{(n+j)\times(n+j)}$ is the diagonal matrix version of the $\boldsymbol{q_E}$ vector, i.e. $\boldsymbol{\Phi} = \text{diag}(\boldsymbol{q_E})$. It is crucial to note that the magnitudes of $\|\boldsymbol{q_E}\|$ and $\lambda_{\mathrm{m}}(\boldsymbol{\Phi})^2$, are produced through real-time computations.

The stiffness optimization problem can thus be represented in the following form:

$$\min/\max\ J_K = \boldsymbol{f_K^T x_K}, \tag{25}$$

thereby attempting to optimise the values of the $\mathrm{H}(\mathbf{K_P})$ matrix, via the modulation of the active stiffness terms contained in $\mathbf{K_P}$. Therefore, the outlined procedure yields positive definite active stiffness matrices. In the above equation:

$$\boldsymbol{f_K} = [1 \ldots 1] \in \mathbb{R}^n, \tag{26}$$

while the optimisation variables vector is defined as:

$$\boldsymbol{x_K} = \left[\mathrm{K}_{P,1} \ldots \mathrm{K}_{P,n}\right] \in \mathbb{R}^n, \tag{27}$$

in view of the fact that $\mathrm{H}(\mathbf{K_P})$ is defined through (7); subject to the constraints:

$$\mathbf{A_K}\boldsymbol{x_K} \leq \boldsymbol{b_K}, \tag{28}$$

which has been elicited by rearranging the conditions expressed by (23) and (24). $\mathbf{A_K} \in \mathbb{R}^{2\times n}$ is of the form:

$$\mathbf{A_K} = \begin{bmatrix} q_{E_{j+1}}^2, \ldots, q_{E\,j+n}^2 \\ -(q_{E_{j+1}}^2, \ldots, q_{E\,j+n}^2) \end{bmatrix}, \tag{29}$$

and contains the products of the multiplication operations performed between the elements of the two $\boldsymbol{q_E}$ vectors, which are then multiplied by the respective diagonal and upper triangular elements of the $\mathrm{H}(\mathbf{K_P})$ matrix. Additionally:

$$\boldsymbol{b_K} = \begin{bmatrix} \beta_K - \psi_K \\ -\zeta_K + \psi_K \end{bmatrix} \in \mathbb{R}^2, \tag{30}$$

with the scalar terms being the following:

$$\beta_K = \left\|\mathbf{K_T} + \mathrm{H}(\mathbf{W_K^{-1}} k_{P_{max}})\right\| \|\boldsymbol{q_E}\|^2,$$
$$\zeta_K = \lambda_m\left(\mathbf{K_T} + \mathrm{H}\left(\mathbf{W_K} k_{P_{min}}\right)\right)\lambda_{\mathrm{m}}(\boldsymbol{\Phi})^2,$$
$$\psi_K = \boldsymbol{q_E^T \mathbf{K_T} q_E}.$$

Thus, the optimization strives to either minimize or maximize the cost function, as part of a procedure that is contingent upon both the robot's divergence/convergence with respect to an equilibrium point, in addition to whether the velocity margin's value is positive or negative. In an ideal scenario, the stiffness value would decrease to its lowest theoretically attainable level once disturbed, thereby maximizing the robot's disturbance absorption capability. Once the disturbance subsides, the stiffness value subsequently increases, conducing to a rapid convergence to the equilibrium point.

B. Online Damping Optimization

The damping regulation process may be realised using a similar approach to that outlined in the previous sub-section, with the caveat that it effectively commences after the execution of each stiffness optimisation procedure, which determines the values of the damping program's bounds. Since a real-time variation of $\mathbf{T_D}$ instantly suggests that the corresponding velocity margin values shall continuously fluctuate, this will unavoidably have an immediate effect on the values of the upper and/or lower bounds, and by extension on the resulting damping gain values. The optimization's objective will be to adjust the magnitude of the Lyapunov derivative's dissipative term, to the extent that it eclipses the energy-injecting term, thus assuring the system's stability. Such a term can be described by equation (81), which has been defined in Appendix D, and is assigned to variable Ω for brevity, as shown below:

$$\Omega(t) = \omega\big(\boldsymbol{q}, \boldsymbol{\theta}, \dot{\boldsymbol{q}}, \dot{\boldsymbol{\theta}}, t\big), \tag{31}$$

where t represents time.

It is notable at this stage, that the energy-injection issue ceases to exist in the divergent case, due to the energy-injecting term's possession of a negative sign $\left(\frac{1}{2}\boldsymbol{q_E^T}\dot{\mathbf{T}}_{\mathbf{D}}(t)\boldsymbol{q_E} \leq 0\right)$, which renders it a dissipative element. For this case, the optimization program may be represented as follows:

- Divergent case

$$\Omega_{div,low}(t) \;\leq\; \Omega(t) \leq \Omega_{div,up}(t), \tag{32}$$

wherein the lower bound, $\Omega_{div,low}(t)$, is computed by means of obtaining the minimum eigenvalue of (81), while replacing the velocity vector, $\dot{\boldsymbol{q}}_{\boldsymbol{F}}$, in (81) with the velocity margin, ν, to assure that the latter would dictate the outcome of the divergent optimisation. Conversely, the upper bound, $\Omega_{div,up}$, is calculated by means of attaining the norm of (81), as shown below:

$$\Omega_{div,low}(t) = \lambda_{\mathrm{m}}\left(\nu^2\boldsymbol{\eta} - \frac{\boldsymbol{q_E^T}\dot{\mathbf{T}}_{\mathbf{D}}\boldsymbol{q_E}}{2}\mathbf{I_{n+j}}\right),$$

$$\Omega_{div,up} = \left\|\begin{bmatrix}\boldsymbol{\eta}_{\mathbf{SAT}} & \mathbf{0}_{(n+j)\times(n+j)} \\ \mathbf{0}_{(n+j)\times(n+j)} & -\frac{\dot{\mathbf{T}}_{\mathbf{D}}}{2}\end{bmatrix}\right\| \left\|\begin{bmatrix}\dot{\boldsymbol{q}}_{\boldsymbol{F}} \\ \boldsymbol{q_E}\end{bmatrix}\right\|^2,$$

where $\mathbf{I_\kappa}$ symbolizes the identity matrix of dimension $\kappa\times\kappa$, and $\boldsymbol{\eta}_{\mathbf{SAT}} = \mathrm{H}(\mathbf{W_D^{-1}}k_{D_{max}} + \mathbf{D})$ is the value of the damping terms matrix norm that brings about saturation. For the purpose of deriving this lower bound, $\mathbf{I_{n+j}}$ is introduced to convert the scalar $\boldsymbol{q_E^T}\dot{\mathbf{T}}_{\mathbf{D}}\boldsymbol{q_E}$ term into a matrix. Moreover, by drawing inspiration from the method proposed in [32], a weighting matrix relying upon the motors' dynamics has been used to perform a gain distribution, as described via the relationship:

$$\mathbf{W_D} = \frac{\sqrt{\mathbf{JK_P}}}{\sqrt{\|\mathbf{JK_P}\|}} \in \mathbb{R}^{n\times n}.$$

Recalling equation (82), the condition expressed via (32), may be written as follows:

$$\Omega_{div,low}(t) - \psi_D \;\leq\; \dot{\boldsymbol{\theta}}^T\mathbf{K_D}\dot{\boldsymbol{\theta}} \leq \Omega_{div,up}(t) - \psi_D, \tag{33}$$

where $\psi_D = \dot{\boldsymbol{\theta}}^T\mathbf{D}\dot{\boldsymbol{\theta}} - \frac{1}{2}\boldsymbol{\theta_E^T}\dot{\boldsymbol{K}}_{\mathbf{P}}\boldsymbol{\theta_E}$.

Contrarily, the program utilised during the convergent phase is the following:

- Convergent case

$$\Omega_{con,low}(t) \;\leq\; \Omega(t) \leq \Omega_{con,up}(t), \tag{34}$$

whose lower bound, $\Omega_{con,low}(t)$, is derived via the individual computation of the minimum eigenvalues of $\begin{bmatrix}\boldsymbol{\eta} & 0 \\ 0 & -\frac{\dot{\mathbf{T}}_{\mathbf{D}}}{2}\end{bmatrix}$, and the diag$\left(\begin{bmatrix}\dot{\boldsymbol{q}}_{\boldsymbol{F}} \\ \boldsymbol{q_E}\end{bmatrix}\right)$ vector, which are contained in equation (82). Moreover, for the divergent case program, the upper bound, $\Omega_{con,up}(t)$, is acquired by exchanging the actual velocity vector with the velocity margin (15) in (82), and subsequently obtaining the norm of the resulting vector, which is multiplied by the norm of $\begin{bmatrix}\boldsymbol{\eta}_{\mathbf{SAT}} & 0 \\ 0 & -\frac{\dot{\mathbf{T}}_{\mathbf{D}}}{2}\end{bmatrix}$, as the following equations demonstrate:

$$\Omega_{con,up}(t) = \left\|\begin{bmatrix}\boldsymbol{\eta}_{\mathbf{SAT}} & \mathbf{0}_{(n+j)\times(n+j)} \\ \mathbf{0}_{(n+j)\times(n+j)} & -\frac{\dot{\mathbf{T}}_{\mathbf{D}}}{2}\end{bmatrix}\right\| \left\|\begin{bmatrix}\boldsymbol{\nu}_{(\boldsymbol{n+j})} \\ \boldsymbol{q_E}\end{bmatrix}\right\|^2,$$

$$\Omega_{con,low} = \lambda_{\mathrm{m}}\left(\begin{bmatrix}\boldsymbol{\eta} & \mathbf{0}_{(n+j)\times(n+j)} \\ \mathbf{0}_{(n+j)\times(n+j)} & -\frac{\dot{\mathbf{T}}_{\mathbf{D}}}{2}\end{bmatrix}\right)\left(\min\left(\begin{bmatrix}\dot{\boldsymbol{q}}_{\boldsymbol{F}} \\ \boldsymbol{q_E}\end{bmatrix}\right)\right)^2.$$

Using a similar manipulation to that resulting in the production of equation (33), the following inequality is obtained:

$$\Omega_{con,low}(t) - \Gamma \;\leq \dot{\boldsymbol{\theta}}^T\mathbf{K_D}\dot{\boldsymbol{\theta}} \leq \Omega_{con,up}(t) - \Gamma.$$

Additionally, the construction of $\Omega_{con,up}(t)$ entails substituting $\dot{\boldsymbol{q}}_{\boldsymbol{F}}$ for ν in (61), and subsequently acquiring the norms of the resulting equation. On the other hand, $\Omega_{con,low}$ is generated by calculating the minimum eigenvalues of (61), having previously transformed the state vector into its matrix form.

By obtaining the velocity, $\dot{\boldsymbol{q}}_{\boldsymbol{F}}$, from the robot's measurements, in an online fashion, the desired bounds on the quadratic damping term $\dot{\boldsymbol{q}}_{\boldsymbol{F}}^{\boldsymbol{T}}\boldsymbol{\eta}\dot{\boldsymbol{q}}_{\boldsymbol{F}}$ can be wrought. The formulation of the damping gain optimization program is then the following:

$$\min/\max\ J_D = \boldsymbol{f}_{\boldsymbol{D}}^{\boldsymbol{T}}\boldsymbol{x}_{\boldsymbol{D}}, \tag{35}$$

where

$$\boldsymbol{f}_{\boldsymbol{D}} = [1 \dots 1] \in \mathbb{R}^n, \tag{36}$$

$$\boldsymbol{x}_{\boldsymbol{D}} = \left[K_{D,1}, \dots K_{D,n}\right] \in \mathbb{R}^n, \tag{37}$$

with δ_i signifying the elements of the overall damping matrix $\boldsymbol{\eta}$ that can be realized via the extraction of its diagonal and upper triangular elements due to its being symmetric; subject to the constraints

$$\mathbf{A}_{\mathbf{D}}\boldsymbol{x}_{\boldsymbol{D}} \leq \boldsymbol{b}_{\boldsymbol{D}}, \tag{38}$$

which results from a manipulation of the conditions expressed by equations (31) and (34), for both of the previously mentioned scenarios. The $\mathbf{A}_{\mathbf{D}} \in \mathbb{R}^{2\times n}$ matrix can be defined in the following manner:

$$\mathbf{A}_{\mathbf{D}} = \begin{bmatrix} \dot{\theta}_{j+1}^2, \dots, \dot{\theta}_{j+n}^2 \\ -\left(\dot{\theta}_{j+1}^2, \dots, \dot{\theta}_{j+n}^2\right) \end{bmatrix}. \tag{39}$$

The $\boldsymbol{b}_{\boldsymbol{D}}$ vector that alternates between values for the two distinct cases, is constructed as follows:

- Divergent case

$$\boldsymbol{b}_{\boldsymbol{D}} = \begin{bmatrix} \Omega_{div,up} - \psi_D \\ -\Omega_{div,low} + \psi_D \end{bmatrix} \in \mathbb{R}^2, \tag{40}$$

- Convergent case

$$\boldsymbol{b}_{\boldsymbol{D}} = \begin{bmatrix} \Omega_{con,up} - \psi_D \\ -\Omega_{con,low} + \psi_D \end{bmatrix} \in \mathbb{R}^2. \tag{41}$$

The merging of the divergent and convergent phase optimisation processes into a unified equation was deemed unfeasible given the current constraints, owing to the difference between their respective state vectors, which necessitated two distinct optimisation routines for the balancing algorithm to alternate between, based on E_{SGN}. Nevertheless, the pursuit of a method that would allow for such a unification is currently being investigated, as it would hasten the overall operation of the algorithm.

V. Alternative Impedance Tuning Techniques

Two supplementary online impedance parameter tuning methods are presented in this section, which pave the way for a direct comparison with the previously proposed bidirectional optimisation scheme.

A. Unidirectional Optimization

The technique expounded in the previous section, functions by optimizing the impedance parameters in the convergent and divergent cases alike. However, the energy-dissipating nature of the impedance-decreasing process was broached earlier, shedding light on the redundancy of the optimization technique for that particular case. It is thus possible to eliminate the optimization procedure from the divergent phase, by switching directly to a fixed set of proportional gains, computed using equation (18). Subsequently, the associated damping gains could be calculated using the following formula:

$$k_{D\,min} = 2\xi_d\sqrt{\lambda_{\mathrm{m}}\left(\mathbf{J}k_{P\,min}\right)}. \tag{42}$$

As a result, both the stiffness and damping optimization processes are deactivated during the divergent phase, and replaced instead by a set of constant proportional and derivative gains computed using equations (18) and (42) respectively.

The approach, which is depicted in Fig. 4, leads to a major simplification of the overall algorithm, as the computational burden of the bilateral optimization is alleviated.

B. Active Impedance Tuning using LSM Constraint

The optimization method introduced in this section, differentiates itself from those previously presented, in the sense that the goal is to exploit the full position tracking performance of the system, while respecting the balancing constraints. To this end, the proposed method strives to replicate maximum joint-level impedance via real-time modulation based on the LSM, as well as on the Lyapunov function's elements, thus obviating the necessity for energy or velocity-margin-based triggers.

The elicitation procedure described henceforth, will revolve around a specific objective, which is no other than the isolation of the proportional gain term. Commencing with equation (12), the entire potential energy function could be segregated on the left-hand side, yielding:

$$V_P \geq \frac{\delta k_v}{2(n_M+1)} - KE, \tag{43}$$

where $KE = \frac{1}{2}\dot{\boldsymbol{q}}_{\boldsymbol{F}}^{\boldsymbol{T}}\mathbf{M}\dot{\boldsymbol{q}}_{\boldsymbol{F}}$. Through the decomposition of the overall stiffness matrix, $\mathbf{T}_{\mathbf{D}}$, into its active and passive constituents, and the explicit definition of the potential energy term V_P, which is the following:

$$V_P = \frac{\boldsymbol{q}_{\boldsymbol{E}}^{\boldsymbol{T}}\mathbf{T}_{\mathbf{D}}\boldsymbol{q}_{\boldsymbol{E}}}{2} + U_g(\boldsymbol{q}) - U_g(\boldsymbol{q}_{\boldsymbol{d}}) + \boldsymbol{q}_{\boldsymbol{E}}^{\boldsymbol{T}}\begin{bmatrix}\boldsymbol{\tau}_{\boldsymbol{g}}(\boldsymbol{q}_{\boldsymbol{d}}) \\ 0\end{bmatrix}, \tag{44}$$

the quadratic active stiffness term may be expressed as follows:

$$\boldsymbol{q}_{\boldsymbol{E}}^{\boldsymbol{T}}\mathrm{H}(\mathbf{K}_{\mathbf{P}})\boldsymbol{q}_{\boldsymbol{E}} \geq K_C, \tag{45}$$

where

$$K_C = 2\left(\frac{\delta K_v}{2(n_M+1)} - KE - U_g(\boldsymbol{q}) + U_g(\boldsymbol{q}_{\boldsymbol{d}}) - \boldsymbol{q}_{\boldsymbol{E}}^{\boldsymbol{T}}\begin{bmatrix}\boldsymbol{\tau}_{\boldsymbol{g}}(\boldsymbol{q}_{\boldsymbol{d}}) \\ 0\end{bmatrix}\right) - \psi_K.$$

The above equation could then serve as a basis for the active stiffness tuning optimisation problem, whose cost function J_{LSM} is defined as follows

$$\max J_{LSM} = \boldsymbol{f}_{\boldsymbol{LSM}}^{\boldsymbol{T}} \boldsymbol{x}_{\boldsymbol{LSM}}, \quad (46)$$

where

$$\boldsymbol{f}_{\boldsymbol{LSM}} = [1 \dots 1] \in \mathbb{R}^l, \quad (47)$$

$$\boldsymbol{x}_{\boldsymbol{LSM}} = \left[\delta_{K_{P_1}}, \dots, \delta_{K_{P_l}}\right] \in \mathbb{R}^l, \quad (48)$$

in which δ_{K_P} denotes the elements of the $\mathrm{H}(\mathbf{K_P})$ matrix; so that the joints' impedance level is continuously maximised.

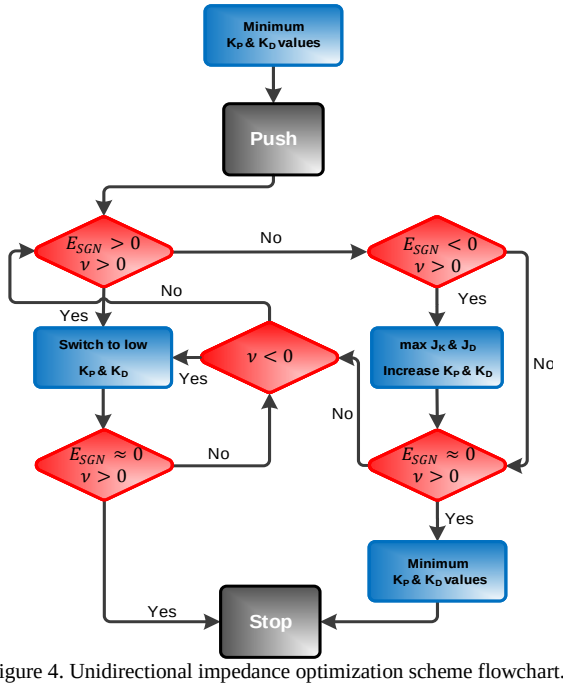

Figure 4. Unidirectional impedance optimization scheme flowchart.

In order to establish a set of limits for the optimisation program, it should firstly be ensured that it conforms to a lower bound constraint, and by subsequently gleaning the various constraint equations, the program may be represented as follows:

$$\lambda_{\mathrm{m}}\left(\mathrm{H}\left(\mathbf{W}_{\mathbf{k}}^{-1} k_{P_{min}}\right)\right) \lambda_{\mathrm{m}}(\boldsymbol{\Phi})^2 \leq \boldsymbol{q}_{\boldsymbol{E}}^{\boldsymbol{T}} \mathrm{H}(\mathbf{K_P}) \boldsymbol{q}_{\boldsymbol{E}} \leq K_C. \quad (49)$$

Despite the fact that this specific optimization constantly attempts to maximize the cost function, the instantaneous active stiffness value could either increase or decrease, since the upper bound is time-varying. Hence, in order to ensure a suppression of the energy-injecting term when the stiffness increases, once this phenomenon has been detected, the damping optimisation program described by equation (35) is simultaneously executed. The active damping for the decreasing stiffness case, could be calculated by exploiting the relationship:

$$K_D = 2\xi_{\mathrm{d}} \sqrt{\mathbf{J}\mathbf{K_P}},$$

where $\mathbf{K_P}$ is the proportional gain matrix calculated using the pertinent optimization.

VI. Impedance Optimization Balancing Experiments

The results acquired during the performance of experiments involving the use of the afore-presented impedance regulation algorithms, are provided in the current section.

A. Experimental Setup Description

As far as its hardware configuration is concerned, the COMAN's lower body comprises 15 DOFs, while standing at a height of 790 mm and weighing 18.9 kg. Each sagittal compliant joint incorporates three position encoders (2 absolute and 1 relative) to measure the link and motor positions, in addition to a torque sensor. The robot is also endowed with a ground contact measurement capability, as it possesses 6-axis force/torque sensors located at its ankles. It is noteworthy that the robot's six sagittal joints are powered by linear SEAs, thus ensuring that a zero-ankle-torque configuration, corresponds to an $X_{CoP} = 0$ position.

In terms of the optimisation technique, the proposed algorithm employs the interior point method to solve the linear programs described throughout the text, whose utilisation still allowed for an available control loop bandwidth of ~3.33 kHz (< 0.3 milliseconds).

B. Bidirectional Optimization Results

The approach described herein was practically validated by means of balancing experiments involving the COMAN's lower body, during which it was manually perturbed while the designed controller attempted to stabilize its structure via the online tuning of its impedance parameters (Fig. 13). The associated video attachment experimentally demonstrates the efficacy of the proposed control scheme, as opposed to utilising fixed low and high gain controllers. The CoP position response arising immediately after the application of an impulsive impact, is displayed in Fig. 5 below, while the time evolutions of the associated stiffness and damping gains, $\mathbf{K_P}$ and $\mathbf{K_D}$ respectively, may also be viewed in Figs. 6-7.

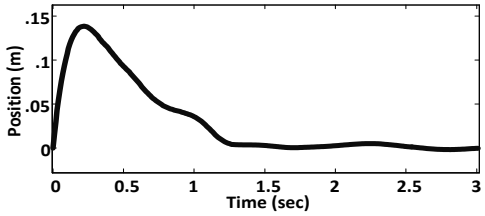

Figure 5. CoP evolution during balancing.

Fig. 8 illustrates the energy variation transpiring over time, computed using $\frac{(V_T(i) - V_T(i-1))}{t_s}$, where t_s symbolises the sampling time, which was set to a value of 1 millisecond in order to slightly exceed the available bandwidth of the control loop. The energy variation term is dependent upon numerous parameters, and is thus predisposed to producing noisy signals, if high levels of quantisation noise are present in its constituent variables. In the latter case, decreasing the sampling time would exacerbate the controller's robustness, as it would result in an amplification of the signal peaks. On the other hand, increasing the sampling time might cause the Energy Variation's noise levels to abate, even though it would

introduce an undesired discrepancy between the evolution of the controller gain variables running on the robot, and the evolution of those same variables comprising the Energy Variation term. It can be observed that once the robot has been perturbed, an increase in the energy variation value occurs, and this action unfolds uninhibitedly until thse energy value reaches a culmination. Subsequently, it begins to decrease, thus signifying a convergence towards the equilibrium point. The change in velocity margin value, $\dot{q}_M$, with respect to time is depicted in Fig. 9, which shows that due to the robot's disturbance from its equilibrium position, the velocity margin value decreases for a period of time, thereby evolving in a converse manner to that of the energy variation shown in Fig. 8. Hence, the velocity margin may only be regarded a margin while it possesses positive values, and may not be perceived as such when residing within the negative value range. The CoP position responses to numerous disturbances, inducing initial velocities spanning the 0.5-2 rad/sec range (considering a 5-10% error margin), are exhibited in Fig. 10, hence demonstrating the controller's capability of rendering the system exceptionally tolerant to external impacts.

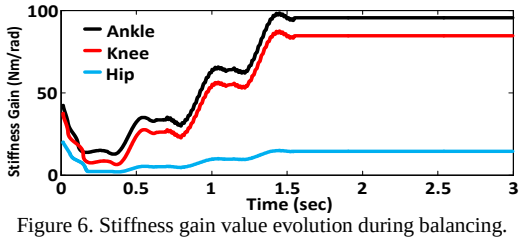

Figure 6. Stiffness gain value evolution during balancing.

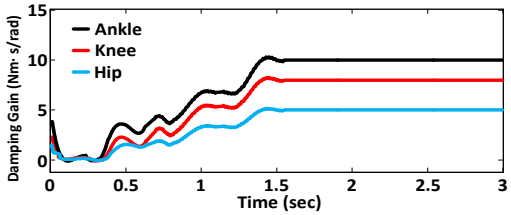

Figure 7. Damping gain value evolution during balancing.

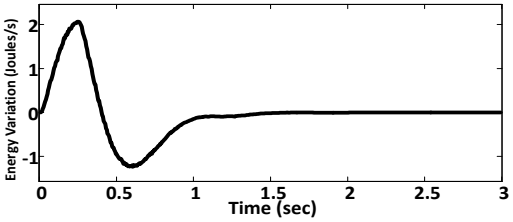

Figure 8. Energy variation during balancing.

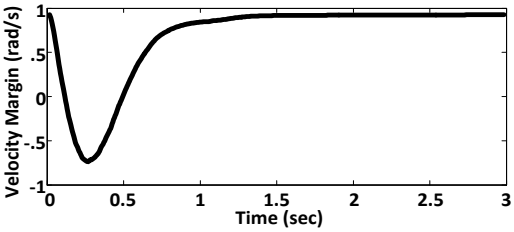

Figure 9. Velocity margin value during balancing.

Similarly, Figs. 11-12 demonstrate the CoP responses to pushes, when employing low impedance (LIC) and high impedance (HIC) controllers respectively. It is noteworthy that the initial velocity values depicted in Figs. 11-12, account for a 5-10% error margin. The LIC outperforms the proposed controller in terms of disturbance rejection, albeit being incapable of driving the robot to the desired equilibrium. HIC on the other hand, possesses a significantly lower perturbation threshold in comparison to the other two controllers, implying that it is more susceptible to losing its balance for the same disturbance magnitudes. It is noteworthy that LIC and HIC utilise the lowest and highest impedance values produced by the optimization controller, respectively.

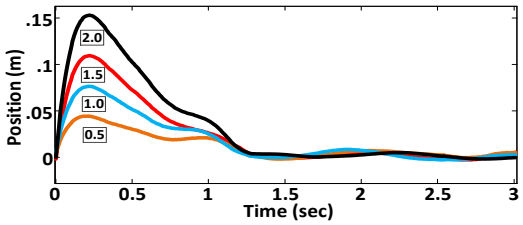

Figure 10. CoP position for 0.5-2 rad/s initial velocities (optimization).

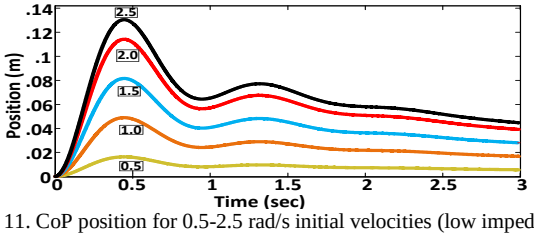

Figure 11. CoP position for 0.5-2.5 rad/s initial velocities (low impedance).

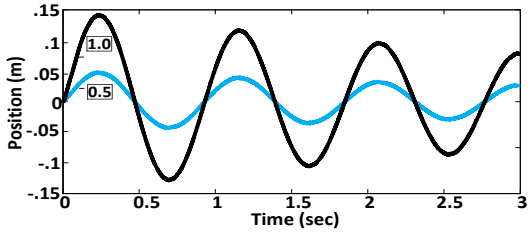

Figure 12. CoP position for 0.5-1 rad/s initial velocities (high impedance).

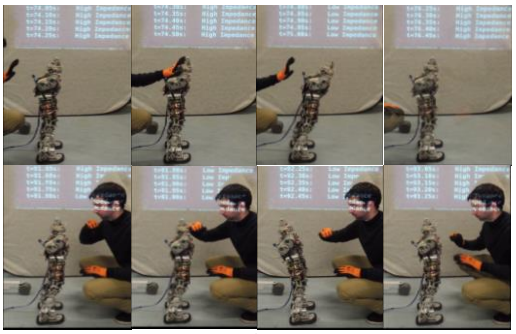
Figure 13. Snapshots of balancing experiments.

C. Unidirectional Optimization Results

This subsection shall focus predominantly on the effect of replacing the bidirectional optimization, with the unidirectional approach outlined in Section V.A. Fig. 14 portrays the CoP response to initial velocities of 0.5-2 rad/s rad/sec (considering a 5-10% error margin), while Fig. 15 isolates the response pertaining to the 1 rad/s initial velocity, whose corresponding stiffness and damping gain evolutions are illustrated in Figs.16 and 17 below. Although a quick inspection allows one to state that the CoP response portrayed in Fig. 15, bears a level of resemblance to that pertaining to

the bidirectional technique, a thorough examination reveals that the settling time of the response is significantly slower in this case. However, the system's impact absorption capability remains intact, as demonstrated in Fig. 15, despite changing the impedance regulation strategy. Moreover, the stiffness and damping gains vary in a distinct manner over time, as depicted in Figs. 16, 17. Likewise, the time evolution of velocity margin shown in Fig. 18, appears to possess positive values over a longer duration, as compared to its counterpart presented in Fig. 9, which consequently implies that the optimization algorithm also remains active for a longer period of time. Despite lacking a noteworthy convergence capability, this specific optimization technique inevitably leads to lower computational costs, by means of obviating the necessity for the execution of a linear programming problem during the divergent phase.

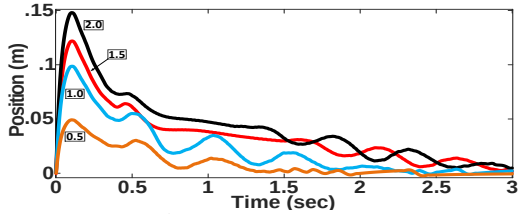

Figure 14. CoP position for 0.5-2 rad/s initial velocities (unidirectional).

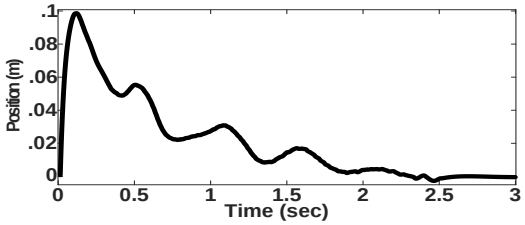

Figure 15. CoP evolution during balancing.

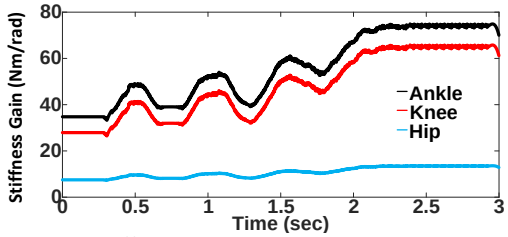

Figure 16. Stiffness gain value evolution during balancing.

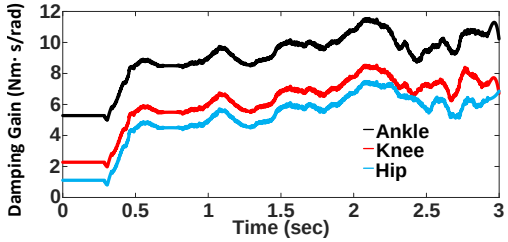

Figure 17. Damping gain value evolution during balancing.

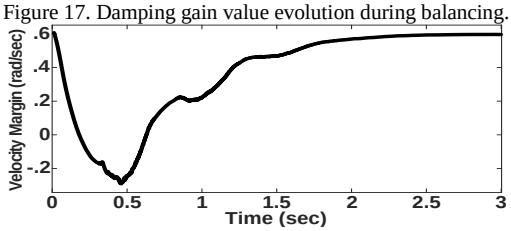

Figure 18. Velocity margin value during balancing (1 rad/s initial velocity).

D. LSM Tuning Results

Finally, this section shall contrast the results obtained when utilizing the LSM-based tuning approach presented in Section V. B., to those acquired using the two previously described techniques. A noteworthy caveat at this stage, is that instead of relying upon the velocity margin variable, this regulation technique operates using a critical quadratic active stiffness variable, namely $\boldsymbol{q}_E^T \mathrm{H}(\mathbf{K_P})\boldsymbol{q}_E$. Fig. 19 clearly reveals that the LSM method yields unsatisfactory results as compared to both optimization methods, as neither the convergence, nor the impact absorption, capabilities, are particularly impressive in comparison to those presented earlier.

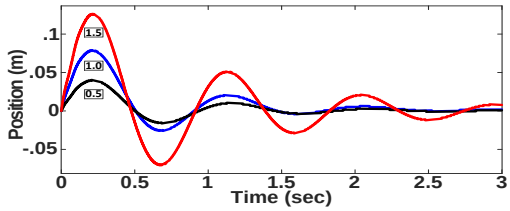

Figure 19. CoP position for 0.5-1.5 rad/s initial velocities (LSM tuning).

This hindrance could be attributed to the method per se, since it relies upon a margin whose value varies in accordance with the kinetic energy term, thus leading to diminishing values of the quadratic active stiffness variable, as the impact magnitude increases. As a result, the impedance tuning procedure remains active for only a brief period of time, as clearly portrayed in Figs. 20-21, where the gain values are essentially set to the lower bounds at a very premature stage. Activating the impedance regulation while the values of this stability variable are negative, would be unreasonable, since such an occurrence renders it impossible to draw a safe conclusion about the robot's state of balance. Fig. 22 represents the evolution of the right-hand side of equation (45), which symbolises a critical stiffness energy, or margin, that is subsequently used to regulate the system's overall stiffness, and by extension, its damping.

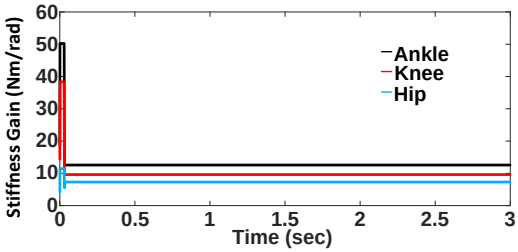

Figure 20. Stiffness gain value evolution during balancing.

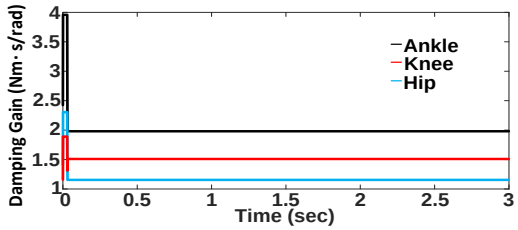

Figure 21. Damping gain value evolution during balancing.

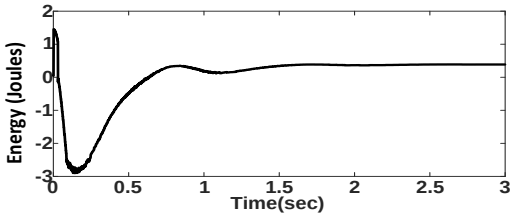

Figure 22. Critical quadratic stiffness energy (1 rad/s initial velocity).

VII. Discussion

The dynamical model described here, has revolved around the use of an over-actuated serial-link mechanism in the frontal plane, which is attributed to the COMAN's possession of mere compliant (SEA) frontal joints, in conjunction with 'stiff' lateral joints. It is for this reason that the proposed algorithm has been directly implemented onto those particular sagittal joints, even though the inclusion of lateral joints in the current model is permissible, and obviates the need for performing any fundamental modelling changes to (1) and (2). However, for the purpose of accounting explicitly for the external contact forces that the system will be subjected to at the foot-ground interface, in the form of a closed kinematic chain, one would need to exploit a contact-force-based three-dimensional compliant model of a humanoid, such as the one presented in [34]. It ought to be noted that model (1), (2) also considers external forces in the form of $\boldsymbol{\tau_{ex}}$, although the explicit double support constraints have been neglected. By following the paradigm outlined in [34], for designing controllers and computing constraint subspaces, it would be possible to generate stiffness and damping gains satisfying the contact constraints, whose online modulation would permit the performance of impedance regulation. Additionally, the construction of a velocity margin, based on the derivation of an LSM, is equally effortless when considering the afore-described model.

VIII. Conclusions

This paper has scrutinized the effect of the online regulation of a humanoid robot's impedance levels, on its balancing capability. The derivation of the velocity margin variable has manifested itself as a crucial stage of the balancing algorithm development, by forging a critical velocity parameter that ultimately dictates the functionality of the entire optimization procedure.

A calculation of the energy function's time derivative, has revealed the existence of an energy-injecting rate of stiffness change term, whose behaviour ought to be suitably repressed by the dissipative element, in an attempt to ensure the system's passivity or stability.

The stiffness tuning technique's operation is primarily dependent on the definition of appropriate bounds, targeted at the performance of either a maximization or minimization of the active stiffness, when converging or diverging with respect to an equilibrium, respectively. Moreover, the active damping tuning procedure's operation is founded upon the afore-described velocity margin, in addition to the energy function's derivative, which is modulated accordingly as a means of guaranteeing stability/passivity. Two supplementary impedance regulation approaches have been contrived, namely the unidirectional optimization and the LSM-based, techniques. These were engineered to facilitate a just comparison with the bidirectional optimization method, which would emphasize the proposed method's superior efficiency in terms of balancing performance.

The experimental results performed using the COMAN, attest to the fact that constant high gain impedance controllers lead to exceedingly low disturbance absorption thresholds, while their low gain counterparts could render a humanoid tolerant to perturbations, albeit lacking a convergence capability. By contrast, the unidirectional optimization algorithm leads to the same heightened disturbance absorption, in spite of its slow convergence, whereas the LSM technique is beleaguered by both weak perturbation rejection, and poor convergence. Consequently, the experimental results shed light on the fact that the proposed impedance regulation scheme could successfully endow a humanoid with both disturbance rejection and convergence capabilities.

IX. Acknowledgements

This work is supported by the WALK-MAN FP7-ICT-2013-10, and the CogIMon H2020-ICT-23-2014, EU projects.

Appendix A

This appendix provides the proof associated with Theorem 1, that has been stated in the paper.

Proof 1: Using (1), (2), (7), and (8), while setting zero velocities and accelerations, gives the following expression (after some algebraic manipulations):

$$\mathbf{T_D}\begin{bmatrix}\boldsymbol{q}-\boldsymbol{q_d}\\ \boldsymbol{\theta}-\boldsymbol{\theta_d}\end{bmatrix}=\begin{bmatrix}\boldsymbol{\tau_g}(\boldsymbol{q})-\boldsymbol{\tau_g}(\boldsymbol{q_d})\\ 0\end{bmatrix}. \tag{50}$$

Letting $\boldsymbol{Q}(\boldsymbol{q_F})=\boldsymbol{q_{F_d}}+\mathbf{T_D^{-1}}\boldsymbol{\tau}(\boldsymbol{q_F})$, where $\boldsymbol{\tau}(\boldsymbol{q_F})=\begin{bmatrix}\boldsymbol{\tau_g}(\boldsymbol{q})-\boldsymbol{\tau_g}(\boldsymbol{q_d})\\ \mathbf{0}\end{bmatrix}$, the contraction mapping theorem [33] yields:

$$\|\boldsymbol{Q}(\boldsymbol{q_F})-\boldsymbol{Q}(\boldsymbol{y})\|\leq\lambda_M(\mathbf{T_D^{-1}})\alpha\|\boldsymbol{q_F}-\boldsymbol{y}\|,$$
$$\therefore\quad \|\boldsymbol{Q}(\boldsymbol{q_F})-\boldsymbol{Q}(\boldsymbol{y})\|\leq\frac{\alpha}{\lambda_m(\mathbf{T_D})}\|\boldsymbol{q_F}-\boldsymbol{y}\|.$$

$\frac{\alpha}{\lambda_m(\mathbf{T_D})}<1$ is a sufficient condition to ensure that (50) has a unique solution, as implied by the following equation:

$$\lambda_m(\mathbf{T_D})>\alpha. \tag{51}$$

It can be demonstrated that (51) has a unique minimum at the equilibrium point $(\boldsymbol{q_d},\boldsymbol{\theta_d})$, by firstly recalling the following potential energy function:

$$V_P=\frac{\boldsymbol{q_E^T}\mathbf{T_D}\boldsymbol{q_E}}{2}+U_g(\boldsymbol{q})-U_g(\boldsymbol{q_d})+\boldsymbol{q_E^T}\begin{bmatrix}\boldsymbol{\tau_g}(\boldsymbol{q_d})\\ 0\end{bmatrix},$$

and by subsequently computing its gradient which produces the following equation:

$$\nabla V_P(\boldsymbol{q},\boldsymbol{\theta},\boldsymbol{q_d},\boldsymbol{\theta_d}) = \mathbf{T_D}\boldsymbol{q_E} + \begin{bmatrix}\boldsymbol{\tau_g}(\boldsymbol{q_d}) - \boldsymbol{\tau_g}(\boldsymbol{q}) \\ 0\end{bmatrix} = 0. \quad (52)$$

From (52), it can be concluded that the Hessian is positive definite and hence (53) has a unique minimum at $(\boldsymbol{q_d},\boldsymbol{\theta_d})$:

$$\nabla^2 V_P(\boldsymbol{q},\boldsymbol{\theta},\boldsymbol{q_d},\boldsymbol{\theta_d}) = \mathbf{T_D} - \begin{bmatrix}\dfrac{\partial \boldsymbol{\tau_g}(\boldsymbol{q})}{\partial \boldsymbol{q}} & 0 \\ 0 & 0\end{bmatrix} > 0. \quad (53)$$

Obtaining the time derivative of the Lyapunov function represented by (10), produces the following result:

$$\dot{V}_T(\boldsymbol{q},\boldsymbol{\theta},\boldsymbol{q_d},\boldsymbol{\theta_d},\dot{\boldsymbol{q}},\dot{\boldsymbol{\theta}},t) = \underbrace{\dot{\boldsymbol{q}}_F^T\begin{pmatrix}\begin{bmatrix}-\mathbf{C} & 0\\ 0 & 0\end{bmatrix}\dot{\boldsymbol{q}}_F + \frac{1}{2}\dot{\mathbf{M}}(\boldsymbol{q})\dot{\boldsymbol{q}}_F \\ +\begin{bmatrix}\boldsymbol{\tau_g}(\boldsymbol{q_d}) - \boldsymbol{\tau_g}(\boldsymbol{q}) \\ 0\end{bmatrix} - \mathbf{T_D}\boldsymbol{q_E} \\ -\begin{bmatrix}0 & 0\\ 0 & \mathbf{D}+\mathbf{K_D}\end{bmatrix}\dot{\boldsymbol{q}}_F + \mathbf{T_D}\boldsymbol{q_E}\end{pmatrix} + \dot{\boldsymbol{q}}_F^T\begin{bmatrix}\boldsymbol{\tau_g}(\boldsymbol{q}) - \boldsymbol{\tau_g}(\boldsymbol{q_d}) \\ 0\end{bmatrix}}_{Constant\ stiffness\ term}$$

$$\underbrace{+\frac{1}{2}\boldsymbol{q}_E^T\dot{\mathbf{T}}_\mathbf{D}\boldsymbol{q}_E}_{Time-varying\ stiffness\ term},$$

which when simplified to a substantial degree using the skew symmetry of $\dot{\mathbf{M}} - \mathbf{2C} = 0$, leads to the expression:

$$\dot{V}_T = -\dot{\boldsymbol{q}}_F^T\boldsymbol{\eta}\dot{\boldsymbol{q}}_F + \frac{1}{2}\boldsymbol{q}_E^T\dot{\mathbf{T}}_\mathbf{D}\boldsymbol{q}_E, \quad (54)$$

where $\boldsymbol{\eta} = \mathrm{H}(\mathbf{D}+\mathbf{K_D})$, ensuing a series of calculations that have been omitted. In this case, it is evident that $\dot{V}_T = 0$ if and only if $\dot{\boldsymbol{q}}_F = 0$. By then substituting $\ddot{\boldsymbol{q}}_F = \dot{\boldsymbol{q}}_F = 0$ into the closed-loop equations (1), (2) and (5), one obtains:

$$\mathbf{S_m^T K}(\mathbf{S_m}\boldsymbol{q} - \boldsymbol{\theta}) = \boldsymbol{\tau_g}(\boldsymbol{q}),$$

$$\mathbf{K}(\boldsymbol{\theta} - \mathbf{S_m}\boldsymbol{q}) = \left(\mathbf{K_P}(\boldsymbol{q_d} - \boldsymbol{\theta}) + \boldsymbol{u_{gc}}\right),$$

which may alternatively be represented in the form of equation (50), whose possession of the unique equilibrium solution $[q_d^T \quad \theta_d^T \quad 0 \quad 0]^T$, was previously demonstrated. Thus, it can be concluded that this is also the largest invariant subset among the set of states yielding $\dot{\boldsymbol{q}}_F = 0$, in which case invocation of LaSalle's theorem leads to the conclusion that the desired equilibrium point is globally asymptotically stable. However, this assumption is only valid when it has been ensured that the following condition holds:

$$\dot{\boldsymbol{q}}_F^T\boldsymbol{\eta}\dot{\boldsymbol{q}}_F \geq \frac{1}{2}\boldsymbol{q}_E^T\dot{\mathbf{T}}_\mathbf{D}\boldsymbol{q}_E, \quad (55)$$

which is what the optimization programs presented throughout the text, shall attempt to achieve.

APPENDIX B

This appendix provides the proof associated with Theorem 2, that has been stated in the main body of text.

Proof 2: Taking the time derivative of the storage function described by (10), while assuming that $\boldsymbol{\tau_{ex}} \neq 0$, then the following relationship arises:

$$\dot{V}_T = \dot{\boldsymbol{q}}_F^T\boldsymbol{\tau_{ex}} - \dot{\boldsymbol{q}}_F^T\boldsymbol{\eta}\dot{\boldsymbol{q}}_F + \frac{1}{2}\boldsymbol{q}_E^T\dot{\mathbf{T}}_\mathbf{D}\boldsymbol{q}_E, \quad (56)$$

which satisfies the passivity inequality:

$$\dot{V}_T = \dot{\boldsymbol{q}}_F^T\boldsymbol{\tau_{ex}} - \dot{\boldsymbol{q}}_F^T\boldsymbol{\eta}\dot{\boldsymbol{q}}_F + \frac{1}{2}\boldsymbol{q}_E^T\dot{\mathbf{T}}_\mathbf{D}\boldsymbol{q}_E \leq \dot{\boldsymbol{q}}_F^T\boldsymbol{\tau_{ex}}, \quad (57)$$

either when,

$$\dot{\boldsymbol{q}}_F^T\boldsymbol{\eta}\dot{\boldsymbol{q}}_F \geq \frac{1}{2}\boldsymbol{q}_E^T\dot{\mathbf{T}}_\mathbf{D}\boldsymbol{q}_E, \quad (58)$$

or when the active stiffness decreases, transforming the energy-injecting term into a dissipative element, as shown below:

$$-\dot{\boldsymbol{q}}_F^T\boldsymbol{\eta}\dot{\boldsymbol{q}}_F - \frac{1}{2}\boldsymbol{q}_E^T\dot{\mathbf{T}}_\mathbf{D}\boldsymbol{q}_E \leq 0.$$

Consequently, this leads to the condition:

$$\dot{V}_T(\boldsymbol{q},\boldsymbol{\theta},\boldsymbol{q_d},\boldsymbol{\theta_d},\dot{\boldsymbol{q}},\dot{\boldsymbol{\theta}},t) = \dot{\boldsymbol{q}}_F^T\boldsymbol{\tau_{ex}}$$
$$-\dot{\boldsymbol{q}}_F^T\boldsymbol{\eta}\dot{\boldsymbol{q}}_F - \frac{\boldsymbol{q}_E^T\dot{\mathbf{T}}_\mathbf{D}\boldsymbol{q}_E}{2} \leq \dot{\boldsymbol{q}}_F^T\boldsymbol{\tau_{ex}}, \quad (59)$$

which clearly satisfies the passivity relationship.

APPENDIX C

The LSM elicitation procedure is provided in the subsequent lines.

The CoP equation corresponding to a humanoid possessing compliant joints, is the following:

$$X_{CoP} = \frac{\tau_a}{m_T g}, \quad (60)$$

where $\tau_a = -\boldsymbol{G}\mathbf{S_m^T K}(\mathbf{S_m}\boldsymbol{q} - \boldsymbol{\theta})$.

By then defining the referential version of the above equation as follows:

$$X_{CoP_d} = \frac{\tau_d}{m_T g}, \quad (61)$$

with $\tau_d = -\boldsymbol{G}\mathbf{S_m^T K}(\mathbf{S_m}\boldsymbol{q_d} - \boldsymbol{\theta_d})$, the statement of an ankle torque error term is permitted as shown below:

$$\tau_a - \tau_d = -\boldsymbol{G}\mathbf{S_m^T K}(\mathbf{S_m}\boldsymbol{q} - \mathbf{S_m}\boldsymbol{q_d} - \boldsymbol{\theta} + \boldsymbol{\theta_d}), \quad (62)$$

$$|\tau_a - \tau_d| \leq \|\boldsymbol{G}\mathbf{S}_\mathbf{m}^\mathrm{T}\mathbf{K}\|\|\mathbf{S}_\mathbf{m}\boldsymbol{q} - \mathbf{S}_\mathbf{m}\boldsymbol{q_d} - \boldsymbol{\theta} + \boldsymbol{\theta_d}\|. \quad (63)$$

Utilizing the triangle inequality then yields:

$$|\tau_a - \tau_d| \leq \|\boldsymbol{G}\mathbf{S}_\mathbf{m}^\mathrm{T}\mathbf{K}\| (\|\mathbf{S}_\mathbf{m}\boldsymbol{q} - \mathbf{S}_\mathbf{m}\boldsymbol{q_d}\| + \|\boldsymbol{\theta} - \boldsymbol{\theta_d}\|),$$

$$|\tau_a - \tau_d| \leq \|\boldsymbol{G}\mathbf{S}_\mathbf{m}^\mathrm{T}\mathbf{K}\| (\|\mathbf{S}_\mathbf{m}\| \, \|\boldsymbol{q} - \boldsymbol{q_d}\| + \|\boldsymbol{\theta} - \boldsymbol{\theta_d}\|). \quad (64)$$

while squaring both sides leads to the equation:

$$|\tau_a - \tau_d|^2 \leq \left\|\boldsymbol{G}\mathbf{S}_\mathbf{m}^\mathrm{T}\mathbf{K}\right\|^2 (\|\mathbf{S}_\mathbf{m}\| \, \|\boldsymbol{q} - \boldsymbol{q_d}\| + \|\boldsymbol{\theta} - \boldsymbol{\theta_d}\|)^2. \quad (65)$$

Given that:

$$2\|\mathbf{S}_\mathbf{m}\|\|\boldsymbol{q} - \boldsymbol{q_d}\|\|\boldsymbol{\theta} - \boldsymbol{\theta_d}\| \leq \|\boldsymbol{q} - \boldsymbol{q_d}\|^2 + \|\mathbf{S}_\mathbf{m}\|^2\|\boldsymbol{\theta} - \boldsymbol{\theta_d}\|^2, \quad (66)$$

it may be stated that:

$$(\|\mathbf{S}_\mathbf{m}\| \, \|\boldsymbol{q} - \boldsymbol{q_d}\| + \|\boldsymbol{\theta} - \boldsymbol{\theta_d}\|)^2 \leq (\|\mathbf{S}_\mathbf{m}\|^2 + 1)(\|\boldsymbol{q} - \boldsymbol{q_d}\|^2 + \|\boldsymbol{\theta} - \boldsymbol{\theta_d}\|^2). \quad (67)$$

Therefore:

$$|\tau_a - \tau_d|^2 \leq \|\boldsymbol{G}\mathbf{S}_\mathbf{m}^\mathrm{T}\mathbf{K}\|^2(\|\mathbf{S}_\mathbf{m}\|^2 + 1)(\|\boldsymbol{q} - \boldsymbol{q_d}\|^2 + \|\boldsymbol{\theta} - \boldsymbol{\theta_d}\|^2),$$

$$|\tau_a - \tau_d|^2 \leq \|\boldsymbol{G}\mathbf{S}_\mathbf{m}^\mathrm{T}\mathbf{K}\|^2 \ (\|\mathbf{S}_\mathbf{m}\|^2 + 1)(\|\boldsymbol{q_E}\|^2). \quad (68)$$

Finally $\|\mathbf{S}_\mathbf{m}\| = \sqrt{n_{max}}$, with $n_{max} = \max_{1\leq i\leq j}(\mathrm{n_i})$, hence:

$$\|\boldsymbol{q_E}\|^2 \geq \frac{1}{n_{max}+1}\left(\frac{|\tau_a - \tau_d|}{\|\boldsymbol{G}\mathbf{S}_\mathbf{m}^\mathrm{T}\mathbf{K}\|}\right)^2. \quad (69)$$

Moreover, the following expression is valid:

$$\left\|\boldsymbol{q}_E^T\mathbf{T_D}\boldsymbol{q_E}\right\| \geq \lambda_\mathrm{m}(\mathbf{T_D})\|\boldsymbol{q_E}\|^2, \quad (70)$$

thus leading to the relationship:

$$\left\|\frac{1}{2}\boldsymbol{q}_E^T\mathbf{T_D}\boldsymbol{q_E}\right\| \geq \frac{1}{2(n_{max}+1)}\lambda_\mathrm{m}(\mathbf{T_D})\left(\frac{|\tau_a - \tau_d|}{\|\boldsymbol{G}\mathbf{S}_\mathbf{m}^\mathrm{T}\mathbf{K}\|}\right)^2. \quad (71)$$

In view of the fact that the $U_g(\boldsymbol{q}) - U_g(\boldsymbol{q_d}) + \boldsymbol{q}_E^T\begin{bmatrix}\boldsymbol{\tau_g}(\boldsymbol{q_d})\\ 0\end{bmatrix}$ terms have been omitted in the analysis presented in the preceding lines, it is now necessary to prove that these terms are smaller than $\frac{1}{2}\boldsymbol{q}_E^T\mathbf{T_D}\boldsymbol{q_E}$. Bearing in mind the previously described property of the potential energy:

$$\left\|\frac{\partial^2 U_g(\boldsymbol{q})}{\partial \boldsymbol{q}^2}\right\| < \alpha,$$

which implies the following relationship:

$$\left\|U_g(\boldsymbol{q}) - U_g(\boldsymbol{q_d}) + \boldsymbol{q}_E^T\begin{bmatrix}\boldsymbol{\tau_g}(\boldsymbol{q_d})\\ 0\end{bmatrix}\right\| \leq \frac{1}{2}\alpha\|\boldsymbol{q} - \boldsymbol{q_d}\|^2, \quad (72)$$

allows one to state that:

$$\left\|U_g(\boldsymbol{q}) - U_g(\boldsymbol{q_d}) + \boldsymbol{q}_E^T\begin{bmatrix}\boldsymbol{\tau_g}(\boldsymbol{q_d})\\ 0\end{bmatrix}\right\| \leq \frac{1}{2}\alpha\|\boldsymbol{q_E}\|^2, \quad (73)$$

$$\therefore \left\|U_g(\boldsymbol{q}) - U_g(\boldsymbol{q_d}) + \boldsymbol{q}_E^T\begin{bmatrix}\boldsymbol{\tau_g}(\boldsymbol{q_d})\\ 0\end{bmatrix}\right\| \leq \frac{\alpha\left\|\boldsymbol{q}_E^T\mathbf{T_D}\boldsymbol{q_E}\right\|}{2\lambda_\mathrm{m}(\mathbf{T_D})}. \quad (74)$$

When considering an arbitrary equilibrium point $\boldsymbol{q_{F_d}}$, V_P could be expressed in the following manner:

$$V_P = \frac{1}{2}\boldsymbol{q}_E^T\mathbf{T_D}\boldsymbol{q_E} + U_g(\boldsymbol{q}) - U_g(\boldsymbol{q_d}) + \boldsymbol{q}_E^T\begin{bmatrix}\boldsymbol{\tau_g}(\boldsymbol{q_d})\\ 0\end{bmatrix}. \quad (75)$$

By relating the above equation to (74), one acquires:

$$V_P \geq \left(1 - \frac{\alpha}{\lambda_\mathrm{m}(\mathbf{T_D})}\right)\frac{\left\|\boldsymbol{q}_E^T\mathbf{T_D}\boldsymbol{q_E}\right\|}{2}, \quad (76)$$

while it is noteworthy that:

$$\frac{\alpha}{\lambda_\mathrm{m}(\mathbf{T_D})} < 1. \quad (77)$$

Through a simplification of (72), one obtains:

$$V_P \geq \frac{1}{2(n_{max}+1)}(\lambda_\mathrm{m}(\mathbf{T_D}) - \alpha)\left(\frac{|\tau_a - \tau_d|}{\|\boldsymbol{G}\mathbf{S}_\mathbf{m}^\mathrm{T}\mathbf{K}\|}\right)^2. \quad (78)$$

The total energy may subsequently be considered, by means of adding the positive (unless $\dot{\boldsymbol{q}}_\boldsymbol{F} = 0$) $\frac{1}{2}\dot{\boldsymbol{q}}_\boldsymbol{F}^T\mathbf{M}(\boldsymbol{q})\dot{\boldsymbol{q}}_\boldsymbol{F}$ term to the potential energy function, which yields:

$$V_T \geq V_P,$$

$$\Rightarrow \qquad V_T \geq \frac{1}{2(n_{max}+1)}\delta\left(\frac{\left|X_{CoP} - X_{CoP_d}\right|m_T g}{\|\boldsymbol{G}\mathbf{S}_\mathbf{m}^\mathrm{T}\mathbf{K}\|}\right)^2,$$

wherein

$$\delta = (\lambda_\mathrm{m}(\mathbf{T_D}) - \alpha) > 0. \quad (79)$$

Finally, the CoP error may be segregated on the left-hand side to attain the following expression:

$$\left|X_{CoP} - X_{CoP_d}\right| \leq \frac{\sqrt{2(n_{max}+1)}\|\boldsymbol{G}\mathbf{S}_\mathbf{m}^\mathrm{T}\mathbf{K}\|}{\sqrt{\delta}m_T g}\sqrt{V_T}. \quad (80)$$

APPENDIX D

Evoking equation (54), and inverting its sign to ensure the extraction of positive damping gains during the pertinent optimisation process, it can be represented as follows:

$$\omega(\boldsymbol{q}, \boldsymbol{\theta}, \dot{\boldsymbol{q}}, \dot{\boldsymbol{\theta}}, t) = \dot{\boldsymbol{q}}_\boldsymbol{F}^T\boldsymbol{\eta}\dot{\boldsymbol{q}}_\boldsymbol{F} - \frac{1}{2}\boldsymbol{q}_E^T\dot{T}_D\boldsymbol{q_E}, \quad (81)$$

where $\boldsymbol{\eta} = \mathrm{H}(\mathbf{D} + \mathbf{K_D})$ is the overall damping matrix and $\dot{\mathbf{T}}_\mathbf{D}$ signifies the derivative of the $\mathbf{T_D}$ matrix. The above matrix could alternatively be displayed as follows:

$$\omega\big(\boldsymbol{q}, \boldsymbol{\theta}, \dot{\boldsymbol{q}}, \dot{\boldsymbol{\theta}}, t\big) = \dot{\boldsymbol{\theta}}^T(\mathbf{D} + \mathbf{K_D})\dot{\boldsymbol{\theta}} - \frac{1}{2}\boldsymbol{\theta}_{\boldsymbol{E}}^{\boldsymbol{T}}\dot{\mathbf{K}}_\mathbf{P}\boldsymbol{\theta}_{\boldsymbol{E}}. \qquad (82)$$

REFERENCES

[1] M. Vukobratovic, B. Borovac, "Zero-moment point – Thirty Five Years of its Life," *Int. J. of Humanoid Robotics, vol. 1, no. 1, pp. 157-173, 2004.*

[2] S. Hyon and G.Cheng, "Passivity-Based Full-Body Force Control for Humanoids and Application to Dynamic Balancing and Locomotion," *Proc. IEEE/RSJ Int. Conf. on Intelligent Robots and Systems, pp. 4915-4922, 2006.*

[3] S. Kajita, K. Tani, "Study of Dynamic Biped Locomotion on Rugged Terrain," *Proc. Int. Conf. on Advanced Robotics, vol. 1, pp. 741-746, 1991.*

[4] B. Stephens, "Humanoid Push Recovery," *Proc. IEEE-RAS Int. Conf. on Humanoid Robots, pp. 589-595, 2007.*

[5] P. Sardain, G. Bessonnet, "Forces Acting on a Biped Robot. Center of Pressure - Zero Moment Point," IEEE Trans. on Systems, Man, and Cybernetics, vol. 34, pp. 630-637, 2004.

[6] N. Hogan, "Impedance Control: An Approach to Manipulation," *American Control Conference, pp. 304-313, 1984.*

[7] Y. Kim, B. Lee, J. Ryu, J. Kim, "Landing Force Control for Humanoid Robot by Time-Domain Passivity Approach," *IEEE Trans. on Robotics, vol. 23, no. 6, pp. 1294-1301, 2007.*

[8] D. P. Losey, A. Erwin, C. G. McDonald, F. Sergi, M. K. O'Malley, "A Time Domain Approach to Control of Series Elastic Actuators: Adaptive Torque and Passivity-Based Impedance Control," *IEEE/ASME Trans. on Mechatronics, 2016.*

[9] T. Sugihara, Y. Nakamura, "Contact phase invariant control for humanoid robot based on variable impedant inverted pendulum model," *Proc. IEEE Int. Conf. on Robotics and Automation, vol. 1, pp. 51-56, 2003.*

[10] J. H. Park, "Impedance control for biped robot locomotion," *IEEE Trans. on Robotics and Automation, vol. 17, no. 6, pp. 870-882, 2001.*

[11] H.-O. Lim, S. A. Setiawan, A. Takanishi, "Balance and impedance control for biped humanoid robot locomotion," *Proc. IEEE/RSJ Int. Conf. on Intelligent Robots and Systems, pp. 494-499, 2001.*

[12] O. Kwon, J. H. Park, "Asymmetric Trajectory Generation and Impedance Control for Running of Biped Robots," *Autonomous Robots, Vol. 26, no. 1, 2009.*

[13] L. Sentis, J. Petersen, R. Philippsen, "Implementation and Stability Analysis of Prioritized Whole-Body Compliant Controllers on a Wheeled Humanoid Robot in Uneven Terrains," *Autonomous Robots, Vol. 35, no. 4, 2013.*

[14] K. Yamamoto, Y. Nakamura, "Switching Feedback Controllers Based on the Maximal CPI Sets for Stabilisation of Humanoid Robots," *Proc. IEEE-RAS Int. Conf. on Humanoid Robots, pp. 549-554, 2009.*

[15] K. Yamamoto, "Resolved COG Viscoelasticity Control of Humanoid Robot," *Proc. IEEE/RSJ Int. Conf. on Intelligent Robots and Systems*, pp. 1364-1371, 2016.

[16] P. M. Wensing, L. R. Palmer, D. E. Orin, "Efficient Recursive Dynamics Algorithms for Operational-Space Control with Application to Legged Locomotion," *Autonomous Robots, Vol. 38, no. 4, 2015.*

[17] E. Spyrakos-Papastavridis, G. Medrano-Cerda, N. G. Tsagarakis, J. S. Dai and D. G. Caldwell, "A Compliant Humanoid Walking Strategy Based on the Switching of State Feedback Gravity Compensation Controllers," *Proc. IEEE/RSJ Int. Conf. on Intelligent Robots and Systems, pp. 3630-3636, 2013.*

[18] N. Van der Noot, A. Ijspeert, R. Ronsse, "Biped gait controller for large speed variations, combining reflexes and a central pattern generator in a neuromuscular model," *Proc. IEEE Int. Conf. on Robotics and Automation, pp. 6267-6274, 2015.*

[19] N. G. Tsagarakis, M. Laffranchi, B. Vanderborght, D. G. Caldwell, "A Compact Soft Actuator for Small Scale Human Friendly Robots," *Proc. IEEE Int. Conf. on Robotics and Automation, pp. 4356-4362, 2009.*

[20] N. G. Tsagarakis, Z. Li, J. Saglia, D. G. Caldwell, "The design of the lower body of the compliant humanoid robot "ccub"," *Proc. IEEE Int. Conf. on Robotics and Automation, pp. 2035-2040, 2011.*

[21] N. G. Tsagarakis, S. Morfey, G. A. Medrano-Cerda, Z. Li and D. G. Caldwell, "Compliant Humanoid COMAN: Optimal Joint Stiffness Tuning for Modal Frequency Control," *Proc. IEEE Int. Conf. on Robotics and Automation, pp. 673-678, 2013.*

[22] F. Ferraguti, C. Secchi, C. Fantuzzi, "A tank-based approach to impedance control with variable stiffness," *Proc. IEEE Int. Conf. on Robotics and Automation, pp.4948-4953, 2013.*

[23] E. Spyrakos-Papastavridis, N. Kashiri, J. Lee, N. G. Tsagarakis, and D. G. Caldwell, "Online Impedance Parameter Tuning for Compliant Biped Balancing," *Proc. IEEE-RAS Int. Conf. on Humanoid Robots, pp. 210-216, 2015.*

[24] E. Spyrakos-Papastavridis, G. Medrano-Cerda, N. G. Tsagarakis, J. S. Dai and D. G. Caldwell, "Gravity Compensation Control of Compliant Joint Systems with Multiple Drives," *Proc. IEEE Int. Conf. on Robotics and Automation, pp.4960-4966, 2013.*

[25] F. Ghorbel, "Modeling and PD Control of Closed-Chain Mechanical Systems," *Proc. IEEE Conf. on Decision & Control, pp. 540-542, 1995.*

[26] F. L. Lewis, C. T. Abdallah, D. M. Dawson, "Control of Robot Manipulators," *NY, USA, Marcel Dekker, 1993, pp. 169-257.*

[27] P. Tomei, "A Simple PD Controller for Robots with Elastic Joints," *IEEE Transactions on Automatic Control, vol. 36, pp. 1208-1213 1991.*

[28] A. de Luca, F. Flacco, "A PD-type regulator with exact gravity cancellation for robots with flexible joints", *Proc. IEEE Int. Conf. on Robotics and Automation, pp. 317-323, 2011.*

[29] J. Pratt, R. Tedrake, "Velocity-based stability margins for fast bipedal walking," *Fast Motions in Biomechanics and Robotics, Springer, pp. 299-324, 2006.*

[30] E. Spyrakos-Papastavridis, N. Perrin, N. G. Tsagarakis, J. S. Dai, and D. G. Caldwell, "Lyapunov stability margins for humanoid robot balancing," *Proc. IEEE/RSJ Int. Conf. on Intelligent Robots and Systems, pp. 945-951, 2014.*

[31] T. Tao, "Topics in Random Matrix Theory," *Graduate Studies in Mathematics, Vol. 132, pp. 46-47, 2012.*

[32] A. Albu-Schäffer, C. Ott, G. Hirzinger "A passivity based cartesian impedance controller for flexible joint robots-part II: Full state feedback, impedance design and experiments," *Proc. IEEE Int. Conf. on Robotics and Automation, pp.2666-2672, 2004.*

[33] H. K. Khalil, *Nonlinear Systems, Third Edition, NJ, USA, Prentice Hall, 2002, pp. 655-656.*

[34] G. Medrano-Cerda, H. Dallali, M. Brown, "Control of a Compliant Humanoid Robot in Double Support Phase: a Geometric Approach," *Int. J. Humanoid Robotics, vol. 09, no. 01, pp. 1250004-1/29, 2012.*